












Research article

# Petrogenesis of Néma 001, an alkali-rich meteorite from the acapulcoite-lodranite parent body

Romain Tartèse<sup>1</sup>  Jérôme Gattacceca<sup>2</sup>  Guillaume Avice<sup>3</sup>  Pierre Beck<sup>4</sup>   
Bertrand Devouard<sup>2</sup>  Vinciane Debaille<sup>5</sup>  Lydia Fawcett<sup>1</sup>  Genevieve Hublet<sup>5</sup>   
Katherine H. Joy<sup>1</sup>  Corinne Sonzogni<sup>2</sup>  Johan Villeneuve<sup>6</sup> 

<sup>1</sup> Department of Earth and Environmental Sciences, The University of Manchester, Oxford Road, Manchester M13 9PL, United Kingdom

<sup>2</sup> CNRS, Aix Marseille University, IRD, INRAE, CEREGE, Aix-en-Provence, France

<sup>3</sup> Université Paris Cité, Institut de Physique du Globe de Paris, CNRS, F-75005 Paris, France

<sup>4</sup> Université Grenoble Alpes, CNRS, IPAG, 38000 Grenoble, France

<sup>5</sup> Laboratoire G-Time, Université libre de Bruxelles, Brussels, Belgium

<sup>6</sup> Université de Lorraine, CNRS, CRPG, UMR7358, F-54000 Nancy, France

✉ Correspondence to: R. Tartèse: [romain.tartese@manchester.ac.uk](mailto:romain.tartese@manchester.ac.uk)

**Author contributions:** Conceptualization: RT, JG; Data curation: RT, JG, GA, PB, BD, VD, LF, GH, KJ, CS, JV; Formal analysis: RT, JG, GA, PB, BD, VD, LF, GH, KJ, CS, JV; Funding acquisition: RT, JG, GA, VD, KJ, JV; Investigation: RT, JG, GA, PB, BD, VD, LF, GH, KJ, CS, JV; Methodology: RT, JG, GA, PB, VD, LF, GH, KJ, CS, JV; Project administration: RT, JG; Resources: JG; Supervision: RT, JG; Validation: RT, JG, GA, PB, VD, LF, GH, KJ, CS, JV; Visualization: RT, GA, PB, VD, KJ, JV; Writing – original draft: RT; Writing – review & editing: JG, GA, PB, BD, VD, KJ, JV;

**Data, code, and outputs:** <https://doi.org/10.48420/29126567.v3>

Submitted: 2025-05-22

Accepted: 2025-09-11

Published: 2025-10-08

Production editor:

Ryan B. Ickert

Handling editor:

Timo Hopp

Reviews:

Two anonymous reviewers

Copyediting:

Elliot Carter, Marthe Klöcking

Primitive achondrites are meteorites characterised by granoblastic textures evidencing high-temperature metamorphism and low degrees of partial melting. These include the acapulcoite and lodranite meteorites, which originated from a common parent body. Acapulcoites experienced low degrees of partial melting (ca. <1 to 5%) and lodranites experienced higher degrees of partial melting (~5-20%). Meteorite collections also include a sample of their chondritic precursor, Grove Mountains 020043, as well as limited examples of partial melting products, such as the mm-sized gabbroic clasts in the Lewis Cliff 86220 transitional acapulcoite-lodranite and the 4.86 g pyroxene-plagioclase coarse-grained Frontier Mountain 93001 meteorite. This suite of samples, thus, provides us with a crucial snapshot into the transition from chondritic material to differentiated planetesimals. Here we propose that the 75.8 g alkali-rich Néma 001 meteorite, a coarse-grained igneous meteorite composed primarily of ortho- and clinopyroxene, plagioclase, and olivine, also originated from the acapulcoite-lodranite parent body. This is supported by a bulk oxygen isotope composition that is undistinguishable from that of the acapulcoites-lodranites and similar ferromagnesian mineral Fe/Mn ratios. Petrological modelling suggests that Néma 001 represents silicate melts formed by ~15% melting of a chondritic precursor similar to Grove Mountains 020043. With the addition of Néma 001, we now have a comprehensive suite of samples from the acapulcoite-lodranite parent body, including chondritic precursor material, residues from ~1-20% partial melting, and variably differentiated igneous rocks. This unique suite of samples is key to further investigate melting and differentiation processes of asteroids, and supports the existence of partially differentiated planetesimals.

## 1 Introduction

In our nascent Solar System, it is thought that refractory calcium- and aluminium-rich inclusions (CAI), chondrules, and micrometre-scale dust migrated towards the mid-plane of the protoplanetary disc and accreted to form the first rocky bodies (e.g., [Dauphas and Chaussidon, 2011](#)). Some

of these early bodies reached a size of a few tens of km in radius and partially or completely melted within ~1.5 Ma after the formation of CAIs due to decay of short-lived radioactive isotopes (<sup>26</sup>Al, <sup>60</sup>Fe) (e.g., [Kleine et al., 2005](#); [Hevey and Sanders, 2006](#)). These types of parent bodies are sampled by the achondrite group of meteorites. Complementing the records of these early melted bodies, chondritic

meteorites provide us with samples of unmelted asteroids, which accreted later than  $\sim 1.5\text{--}2$  Ma after the CAIs formed (Mason, 1967; Kleine et al., 2005, 2009; Hevey and Sanders, 2006; Sugiura and Fujiya, 2014). In practice this top level distinction between achondrites and chondrites sampling differentiated and unmelted bodies, respectively, is overly simplistic. For instance, palaeomagnetism studies suggest that chondrites from a range of groups (CV, R, and ordinary) may represent the undifferentiated crust of planetesimals with partially to fully melted interiors (Gattacceca et al., 2016; Bryson et al., 2019; Cournède et al., 2020; Carporzen et al., 2011; Elkins-Tanton et al., 2011; Weiss and Elkins-Tanton, 2013).

The primitive achondrite meteorites provide us with a crucial snapshot into the transition from unmelted chondritic material to differentiated bodies. These primitive achondrites typically have bulk compositions similar to chondrites, but are characterised by achondrite textures generally interpreted as resulting from low degrees of partial melting (e.g., Krot et al., 2014). The acapulcoite and lodranite meteorites are primitive achondrites that are thought to originate from a common parent body, and to represent residues of ca. 1 to 20% partial melting of a chondritic precursor (Mittlefehldt et al., 1996; McCoy et al., 1997a,b; Floss, 2000; Keil and McCoy, 2018; Lucas et al., 2022). Acapulcoites have experienced very low degrees of partial melting (ca.  $<1$  to 5%) at temperatures of  $\sim 950$  to  $1100$  °C. They are fine-grained ( $< 500$   $\mu\text{m}$ ) rocks typically displaying granular textures. Lodranites are characterised by larger grain sizes ( $\geq 500$   $\mu\text{m}$ ) than acapulcoites, having experienced higher degrees of partial melting ( $\sim 5$  to 20%) deeper in their parent body at temperatures of  $\sim 1100$  to  $1250$  °C (Mittlefehldt et al., 1996; McCoy et al., 1997a,b; Floss, 2000; Dhaliwal et al., 2017; Keil and McCoy, 2018; Lucas et al., 2022). Based on similar mineral chemistry, and oxygen and chromium isotope compositions, it is likely that we have a sample of the chondritic precursor of the acapulcoites-lodranites: the type 4 chondrite Grove Mountains (GRV) 020043 (Li et al., 2018; McCoy et al., 2019). Detailed studies of the mineralogy and mineral minor and trace element variations of acapulcoites and lodranites also indicate that silicate melts were extracted from lodranite precursors and interacted with the overlying acapulcoite and acapulcoite-lodranite transitional horizons, as represented by gabbroic clasts in Lewis Cliff (LEW) 86220 acapulcoite and the 4.86 g Opx-Cpx-Plag coarse-grained Frontier Mountain (FRO) 93001 meteorite (e.g., McCoy et al., 1997b; Folco et al., 2006; Lucas et al., 2022).

A few ungrouped achondrite meteorites show that partial melting of chondritic material in the first few million years of evolution of the Solar System produced alkali-rich melts with broadly andesitic compositions. These achondrites include Erg Chech 002 (Barrat et al., 2021), Grave Nunataks (GRA) 06128/06129 (Day et al., 2009, 2012; Shearer et al., 2010), and the evolved clast ALM-A from the Almahata Sitta polymict meteorite (Bischoff et al., 2014). These last two meteorites have been genetically linked to the brachinite and ureilite asteroidal parent bodies, respectively. Here we

describe the mineralogy and geochemistry of the meteorite Néma 001, which was found in 2021 in the Mauritanian Sahara Desert, and show that its characteristics are consistent with its formation by partial melting of a chondritic precursor for which the acapulcoite-lodranite meteorites represent partial melting residues. We propose that altogether the type 4 chondrite GRV 020043, acapulcoites, lodranites, and Néma 001 provide us with the first complete sample suite linking chondritic and differentiated achondritic materials from a single parent asteroid.

## 2 Methods

### 2.1 Bulk oxygen isotope analysis

The triple oxygen isotope composition of a  $\sim 2.1$  mg aliquot of a powdered assemblage of a dozen grains totalling 7 mg was carried out at the Stable Isotopes Laboratory (PANISS) of CEREGE (Aix-en-Provence, France) using a laser fluorination line coupled to a Delta V Plus ThermoFisher Isotope Ratio Mass Spectrometer (IR-MS). More specifically,  $\text{O}_2$  was first extracted using a laser-heating fluorination technique (Alexandre et al., 2006; Suavet et al., 2010; Outrequin et al., 2021), followed by a cryogenic purification with a slush at  $-114$  °C to remove any molecule interfering with the mass 33 (e.g., NF for example). The gas was then directly sent to the dual-inlet mass spectrometer. The oxygen isotope results are expressed in ‰ versus the international reference standard V-SMOW. The  $\delta^{18}\text{O}$  and  $\delta^{17}\text{O}$  values of the reference gas were calibrated with measurements of a NBS 28 standard ( $\delta^{18}\text{O} = 9.570$  ‰;  $\delta^{17}\text{O} = 4.991$  ‰;  $\Delta^{17}\text{O} = 0$  ‰, where  $\Delta^{17}\text{O} = \delta^{17}\text{O} - 0.52 \times \delta^{18}\text{O}$ ; Wostbrock and Sharp, 2021). The sample measurements were corrected on a daily basis using a 1.5 mg quartz internal laboratory standard “Boulangé” (Alexandre et al., 2006; Suavet et al., 2010; Outrequin et al., 2021). The triple oxygen isotope composition of silicates is expressed on the Vienna Standard Mean Ocean Water-Standard Light Antarctic Precipitation (VSMOW-SLAP) scale as recommended by Wostbrock and Sharp (2021). The reproducibility of the measurements of the quartz laboratory standard was 0.16, 0.09, and 0.011 ‰ for  $\delta^{18}\text{O}$ ,  $\delta^{17}\text{O}$ , and  $\Delta^{17}\text{O}$ , respectively ( $1\sigma$  uncertainties,  $n = 6$ ).

### 2.2 Whole rock trace element analysis

After sawing the main mass of Néma 001 (ca.  $3 \times 4$  cm in size; Figure 1) with a diamond wire saw, we recovered 606 mg of dust. Around 40 mg of this representative dust was digested at  $120$  °C for 48 h on a hot plate in PFA beaker using distilled concentrated HF and  $\text{HNO}_3$  acid in proportion 1:3 at the Laboratoire G-Time at Université Libre de Bruxelles (ULB). After evaporation, concentrated distilled HCl was added for 48 h on hot plate at  $120$  °C. The solution was clear after this treatment, and the sample was evaporated and redissolved in  $\text{HNO}_3$  (5%) for dilution before analyses. Synthetic standards were used for preparing a calibration curve and USGS BHVO-2 standard was used for checking reproducibility and accuracy. Samples were doped

with In for monitoring and correcting possible instrumental drift. Internal reproducibility was better than 7% for all elements (RSD) (see Table S1, [Tartèse et al., 2025](#)). Note that there is likely some contamination from the sawing blade for elements such as Fe, Co, Ni, Cu, and Cr.

### 2.3 Scanning electron microscopy

We acquired backscatter electron (BSE) images and X-ray chemical maps of the Néma 001 polished section using the Oxford instrument Aztec software on a Hitachi benchtop scanning electron microscope (SEM) at the University of Manchester.

### 2.4 Electron probe microanalysis

Quantitative major elements analyses of minerals were obtained using a Cameca SX100 electron microprobe at Université Pierre et Marie Curie (UPMC) CAMPARIS facility. The operating conditions were 15 kV accelerating voltage with a current of 15 nA and a counting time of 30 s, with a focused beam (1  $\mu\text{m}$ ). Both natural and synthetic standards were used for calibration: albite for Na; anorthite for Al; apatite for P; diopside for Mg, Si, Ca; orthoclase for K; pyrite for S; MnTiO<sub>3</sub> for Mn and Ti; Cr<sub>2</sub>O<sub>3</sub> for Cr; Fe<sub>2</sub>O<sub>3</sub> for Fe; NiO for Ni; vanadinite for V<sub>2</sub>O<sub>5</sub>; and Zn for ZnO. The detection limits were 324  $\mu\text{g.g}^{-1}$  for K, 327  $\mu\text{g.g}^{-1}$  for Ca, 453  $\mu\text{g.g}^{-1}$  for S, 461  $\mu\text{g.g}^{-1}$  for Al, 475  $\mu\text{g.g}^{-1}$  for Na, 593  $\mu\text{g.g}^{-1}$  for Si, 610  $\mu\text{g.g}^{-1}$  for Mg, 649  $\mu\text{g.g}^{-1}$  for P, 809  $\mu\text{g.g}^{-1}$  for Mn, 1134  $\mu\text{g.g}^{-1}$  for Ni, 1234  $\mu\text{g.g}^{-1}$  for Fe, 1270  $\mu\text{g.g}^{-1}$  for Cr, 1596  $\mu\text{g.g}^{-1}$  for Ti, and 3260  $\mu\text{g.g}^{-1}$  for Co. All analyses with oxide totals outside of the range 98.5–101 wt% were discarded. Results are reported in Table S2 ([Tartèse et al., 2025](#)).

### 2.5 Reflectance spectroscopy

Bi-directional reflectance spectra were obtained on about 100 mg of powder and on an epoxy-mounted polished slab of Néma 001. Powder measurements as well as point spectra on the thick section were obtained with the SHADOWS instrument at the Institut de Planétologie et d'Astrophysique de Grenoble ([Potin et al., 2018](#)) in the 0.5–2.6  $\mu\text{m}$  range. Reflectance spectra were obtained at a phase angle of 20°, with a spot size of 6 mm in diameter, and normalised with Spectralon<sup>TM</sup> and Infragold<sup>TM</sup>. The spectral sampling is 10 nm with a spectral resolution of 3 to 10 nm across the spectral range. Because of the presence of resin in the thick section, we used a spectrum obtained on a feldspar-rich area (that should be featureless in this spectral range or with very weak bands) to identify and correct organic absorption bands related to the resin. This resin signature was removed from spectra measured on clinopyroxene-rich and olivine-rich areas.

### 2.6 Laser ablation – inductively coupled plasma mass spectrometry

#### 2.6.1 Minor and trace element analysis

Trace element abundances were determined in plagioclase, clinopyroxene, orthopyroxene, and olivine in Néma 001 at

The University of Manchester, using a Teledyne Photon Machines Analyte Excite+ 193 nm ArF Excimer laser ablation system with a HelEx II active 2-volume ablation cell, coupled to an Agilent 8900 ICP-MS using a Squid signal-smoothing device (see Table S3, [Tartèse et al., 2025](#), for a summary of the analytical setup and data processing procedure).

Silicates were analysed using a spot size of 85  $\mu\text{m}$ , a fluence of 4  $\text{J.cm}^{-2}$ , and a repetition rate of 5 Hz. Each analysis lasted 40 s and was preceded by 20 s counting time of the gas blank (background). We analysed the following masses (with dwell time in ms in brackets): <sup>7</sup>Li (10), <sup>23</sup>Na (10), <sup>26</sup>Mg (5), <sup>27</sup>Al (5), <sup>29</sup>Si (5), <sup>39</sup>K (10), <sup>44</sup>Ca (5), <sup>45</sup>Sc (10), <sup>47</sup>Ti (10), <sup>51</sup>V (10), <sup>52</sup>Cr (10), <sup>55</sup>Mn (10), <sup>57</sup>Fe (10), <sup>59</sup>Co (10), <sup>60</sup>Ni (10), <sup>63</sup>Cu (10), <sup>66</sup>Zn (10), <sup>71</sup>Ga (10), <sup>85</sup>Rb (10), <sup>88</sup>Sr (10), <sup>89</sup>Y (10), <sup>90</sup>Zr (10), <sup>93</sup>Nb (10), <sup>95</sup>Mo (10), <sup>133</sup>Cs (10), <sup>137</sup>Ba (10), <sup>139</sup>La (20), <sup>140</sup>Ce (20), <sup>141</sup>Pr (20), <sup>146</sup>Nd (20), <sup>147</sup>Sm (20), <sup>153</sup>Eu (20), <sup>157</sup>Gd (20), <sup>159</sup>Tb (20), <sup>163</sup>Dy (20), <sup>165</sup>Ho (20), <sup>166</sup>Er (20), <sup>169</sup>Tm (20), <sup>172</sup>Yb (20), <sup>175</sup>Lu (20), <sup>208</sup>Pb (10), <sup>232</sup>Th (10), and <sup>238</sup>U (10). Signal intensities were corrected from background contributions by subtracting the gas blank.

The Trace Elements data reduction scheme of the Iolite v4.8 software ([Paton et al., 2010](#)) was used for data reduction, using known Si abundances for reference materials ([Jochum et al., 2005](#); [Woodhead and Hergt, 2000](#)) and those measured by EPMA for Néma 001 silicates for internal standardisation. Silicate analyses were bracketed by analysing USGS reference glasses BHVO-2G, BIR-1G, and BCR-2G every ~10–15 unknown analyses. USGS glass BIR-1G was used as the primary reference material (except for <sup>238</sup>U for which we used BCR-2G), while glasses BHVO-2G and BCR-2G were treated as unknowns and used as quality control reference materials. For most of the elements analysed, accuracy is typically within  $\pm 10\%$  of recommended values for the BHVO-2G and BCR-2G USGS reference glasses, and better than  $\pm 5\%$  for REE (see Table S4, [Tartèse et al., 2025](#)). The combination of a large spot size of 85  $\mu\text{m}$ , a moderate fluence of 5  $\text{J.cm}^{-2}$ , and total laser shot counts of < 250, was used to minimise fractionation effects between silicate minerals and silicate glass calibration materials ([Bussweiler et al., 2019](#)). All data are given in Table S4 ([Tartèse et al., 2025](#)), together with their associated 2 standard error uncertainties and detection limits calculated using the method of [Howell et al. \(2013\)](#).

#### 2.6.2 Apatite U-Pb dating

Apatite U-Pb dating and rare earth element (REE) analyses were carried out simultaneously at the University of Manchester using a Teledyne Photon Machines Analyte Excite+ 193 nm ArF excimer laser ablation system equipped with a HelEx II active 2-volume ablation cell, coupled to an Agilent 8900 triple quadrupole Inductively Coupled Plasma Mass Spectrometer (ICP-MS) using a Squid signal-smoothing device. A summary of the analytical setup and data processing procedure is provided in Table S5 ([Tartèse et al., 2025](#)).

The material ablated from target apatite was carried to the ICP-MS by high purity He, which was mixed with Ar

before injection into the plasma source. High purity  $N_2$  was added to the He stream at a flow rate of 2.5 mL/min to enhance sensitivity. Tuning of the ICP-MS and mass calibration were performed at the start of the analytical session by optimising the ion signals during ablation of the NIST SRM 612 reference glass, while maintaining  $^{238}U^+/^{232}Th^+$  close to unity and minimising the  $^{232}Th^{16}O^+/^{232}Th^+$  ratio (ca. 0.17%).

Apatite was ablated using a 65  $\mu m$  circular spot size, a fluence of 5 J.cm<sup>2</sup>, and a repetition rate of 6 Hz. Each analyses lasted 40 s and was preceded by 20 s counting time of the gas blank (background). We analysed the following masses (with dwell time in ms in brackets):  $^{31}P$  (5),  $^{44}Ca$  (5),  $^{89}Y$  (10),  $^{139}La$  (10),  $^{140}Ce$  (10),  $^{141}Pr$  (10),  $^{146}Nd$  (10),  $^{147}Sm$  (10),  $^{153}Eu$  (10),  $^{157}Gd$  (10),  $^{159}Tb$  (10),  $^{163}Dy$  (10),  $^{165}Ho$  (10),  $^{166}Er$  (10),  $^{169}Tm$  (10),  $^{172}Yb$  (10),  $^{175}Lu$  (10),  $^{202}Hg$  (10),  $^{204}Pb$  (20),  $^{206}Pb$  (30),  $^{207}Pb$  (50),  $^{208}Pb$  (10),  $^{232}Th$  (10),  $^{238}U$  (30).

For U-Pb data reduction, we used the Madagascar (Mad) apatite standard (ID-TIMS age of  $473.5 \pm 0.7$  Ma; [Cochrane et al., 2014](#)) as our primary reference material, and the MRC-1 apatite (ID-TIMS age of  $153.4 \pm 0.4$  Ma; [Apen et al., 2022](#)), the BRZ-1 apatite (ID-TIMS age of  $2078 \pm 12$  Ma [Apen et al., 2022](#)), Duluth Complex FC1 apatite ( $1078 \pm 12$  Ma; [Härtel et al., 2023](#)), and Durango apatite ( $32.7 \pm 0.1$  Ma; [Paul et al., 2021](#)) treated as unknown for quality control. Raw data were corrected for background, mass bias, and U-Pb downhole fractionation using the VizualAge UComPbine routine in the Lolite v4.8 software ([Paton et al., 2010](#); [Petrus and Kamber, 2012](#); [Chew et al., 2014](#)). We obtained intercept dates of  $155.2 \pm 1.3$  Ma for MRC-1 ( $2\sigma$ ,  $n = 8$ , MSWD = 1.9, anchored at a common  $^{207}Pb/^{206}Pb$  of 0.85; [Apen et al., 2022](#)),  $2115 \pm 10$  Ma for BRZ-1 ( $2\sigma$ ,  $n = 8$ , MSWD = 2.4, anchored at a common  $^{207}Pb/^{206}Pb$  of 1.14; [Apen et al., 2022](#)),  $1059 \pm 15$  Ma for FC1 ( $2\sigma$ ,  $n = 6$ , MSWD = 0.4, unanchored and yielding a common  $^{207}Pb/^{206}Pb$  of  $0.90 \pm 0.04$  identical to known ratio; [Härtel et al., 2023](#)), and  $33.9 \pm 0.7$  Ma for Durango ( $2\sigma$ ,  $n = 8$ , MSWD = 1.1, anchored at a common  $^{207}Pb/^{206}Pb$  of 0.8615; [Paul et al., 2021](#)), which are consistent with known U-Pb ages of these reference materials. For REE data reduction, we used the Durango apatite as our primary reference material (using the trace element abundances given in [Chew et al., 2016](#)), and the Trace Element data reduction scheme of the Lolite v4.8 software ([Paton et al., 2010](#)), with  $^{31}P$  as an internal standard and a nominal P abundance of 41.2 wt% for all apatite analyses. All results are provided in Tables S6 (U-Pb dating) and S7 (REE analyses) of [Tartèse et al. \(2025\)](#).

## 2.7 Secondary ion mass spectrometry

Mg isotope compositions and Al/Mg concentration ratios were measured with the CAMECA IMS 1280-HR2 ion microprobe at CRPG-CNRS in Nancy (France).

**Feldspar settings** Because of the very low Mg content of the feldspars, measurements were made in monocollection mode using the central electron multiplier (EM) for  $^{24}Mg^+$ ,

$^{25}Mg^+$ , and  $^{26}Mg^+$  and the central Faraday cup (FC2) for  $^{27}Al^+$ . The samples were sputtered with a  $\sim 5$  nA  $O^-$  primary beam rastered over  $15 \times 15 \mu m$ . The transfer optic magnification was set at 80  $\mu m$  to ensure an efficient instrumental transmission and to fully fill the field aperture set at 2500  $\mu m$ . The mass resolving power (MRP) was set at  $M/\Delta M \sim 2500$  in order to completely remove the  $^{24}MgH^+$  interference on  $^{25}Mg^+$ . One measurement consisted of a 90 s preanalysis sputtering to clean the sample surface and attain stable count rates on detectors followed by automatic secondary beam and energy centering, and 40 cycles with counting times during each cycle of 4, 5, 10, 10, 3, and 2 s at masses 23.8 (background for EM),  $^{24}Mg$ ,  $^{25}Mg$ ,  $^{26}Mg$ , 26.8 (background for FC2) and  $^{27}Al$ , respectively. Miyake-Jima plagioclase ( $^{27}Al/^{24}Mg = 347$ , determined by LA-ICP-MS for the crystal used here) was used to calibrate the instrumental isotopic fractionation and the relative Al/Mg ion yield. Two sigma standard errors on the mean of  $\pm 4$ –5‰ for  $\delta^{25}Mg$ ,  $\delta^{26}Mg$ , and  $\delta^{26}Mg^*$  were obtained for the standard. The relative Al/Mg ion yield was determined to be  $1.13 \pm 0.02$ . Typical counts rates for Néma 001 feldspars were 6000 cps, 750 cps, 800 cps, and  $3 \times 10^7$  cps for  $^{24}Mg$ ,  $^{25}Mg$ ,  $^{26}Mg$ , and  $^{27}Al$ , respectively. The uncertainties reported for the measurements of the samples are  $2\sigma$  uncertainties calculated by summing in a quadratic way the uncertainties due to counting statistic for each analysis and the uncertainties related to calibration of instrumental isotopic fractionation and Al/Mg ion yield.

**Olivine settings** The measurements were made in multi-collection mode using four off-axis FCs, L1, C, H1, and H'2 for  $^{24}Mg^+$ ,  $^{25}Mg^+$ ,  $^{26}Mg^+$ , and  $^{27}Al^+$ , respectively (see [Piralla et al., 2023](#), for details). The samples were sputtered with a  $\sim 10$  nA  $O^-$  primary beam rastered over  $5 \times 5 \mu m$ . The transfer optic magnification was set at 80  $\mu m$  to insure an efficient instrumental transmission and to fully fill the field aperture set at 2500  $\mu m$ . The MRP was set at  $M/\Delta M \sim 2500$  (slit 1) in order to completely remove the  $^{24}MgH^+$  interference on  $^{25}Mg^+$ . One measurement consisted of a 90 s preanalysis sputtering to clean the sample surface and attain stable count rates on detectors, during which offsets of FCs were measured, followed by automatic secondary beam and energy centering, and 40 cycles of 5 s integration time for data acquisition. San Carlos olivine, Gold Enstatite, CLDR01 glass, and Ipanko-4 Spinel were used to calibrate the instrumental isotopic fractionation and the relative Al/Mg ion yield. Two sigma standard errors on the mean of  $\pm 0.04$ ‰,  $\pm 0.04$ ‰, and  $\pm 0.04$ ‰ for  $\delta^{25}Mg$ ,  $\delta^{26}Mg$ , and  $\delta^{26}Mg^*$ , respectively, were obtained for the standards. The relative Al/Mg ion yield was determined to be  $0.801 \pm 0.009$ . The uncertainties reported for the measurements of the samples are  $2\sigma$  uncertainties calculated by summing in a quadratic way the uncertainties due to counting statistic for each analysis and the uncertainties related to calibration of instrumental isotopic fractionation and Al/Mg ion yield (Table S8, [Tartèse et al., 2025](#)).

The Mg isotope compositions are given in delta notation according to:  $\delta^{25}Mg_X = \ln[(^{25}Mg/^{24}Mg)_X / (^{25}Mg/^{24}Mg)_R] \times 1000$  (similarly for  $^{26}Mg$ ) with  $R$  referring to the ratio for



SRM 980 from Galy et al. (2003). The  $^{26}\text{Mg}$  excesses due to  $^{26}\text{Al}$  decay are denoted  $\delta^{26}\text{Mg}^*$  with  $\delta^{26}\text{Mg}^* = \delta^{26}\text{Mg} - \delta^{25}\text{Mg}/\beta$  (with  $\beta = 0.511$ , corresponding to kinetic mass fractionation of Mg isotopes). Note that the choice of the mass fractionation law is not critical to the current data set since the degree of intrinsic mass fractionation is small and most likely due to imperfectly corrected matrix effects in feldspars (Table S8, Tartèse et al., 2025), and because the Al/Mg ratios of feldspar that control the isochron are high enough for the uncertainty introduced by the choice of fractionation law to be insignificant. The  $(^{26}\text{Al}/^{27}\text{Al})_0$  and  $\delta^{26}\text{Mg}^*_0$  were calculated from the isochron regression fitted using the IsoPlot software (Vermeesch, 2018). The  $^{26}\text{Al}$ - $^{26}\text{Mg}$  relative age was calculated using the canonical  $^{26}\text{Al}/^{27}\text{Al}$  ( $5.23 \times 10^{-5}$ ; Jacobsen et al., 2008) and a  $^{26}\text{Al}$  half-life of 0.717 Ma (Basunia and Hurst, 2016).

## 2.8 Wet chemistry and Mg isotope mass spectrometry

Wet chemistry was performed at the Laboratoire G-Time at Université Libre de Bruxelles (ULB) on a bulk rock aliquot and three mineral separate fractions (orthopyroxene, clinopyroxene, plagioclase). Samples were digested in 1:3 distilled concentrated HF:HNO<sub>3</sub>, and, after evaporation, followed by three steps in distilled concentrated HNO<sub>3</sub>. Solutions were clear after those steps. A 0.5% aliquot was taken from the bulk sample to measure  $^{27}\text{Al}/^{24}\text{Mg}$  ratios on the Agilent 7700 ICP-MS at Laboratoire G-Time at ULB. Measurements were calibrated using different standard solutions gravimetrically prepared with different Al/Mg ratios representing the range measured in the present study (Al:Mg of 0:10; 1:10; 1:100; 100:1; 100:10; 100:20 and 200:0.5). Indium and Sc were used as internal standards. Each  $^{27}\text{Al}/^{24}\text{Mg}$  ratio reported in Table S8 (Tartèse et al., 2025) is the average of 5 individual measurements and the quoted uncertainties are 2SE.

Magnesium was purified using cation-exchange resin AG50W-X12 in 0.4 cm diameter  $\times$  20 cm length columns. The procedure from Hublet et al. (2017) was slightly modified by doubling the length of the column. The first step was made in 1 mol l<sup>-1</sup> HNO<sub>3</sub> while the second step used a mixture of 1 mol l<sup>-1</sup> HNO<sub>3</sub>: 0.1 mol l<sup>-1</sup> HF to ensure the total removal of major cations (Ca, Na, Fe, Ti) with a yield better than 95%.

Magnesium isotope ratios were measured on the CC-MC-ICP-MS Nu Instruments Sapphire at ULB in wet mode and low resolution. Samples were introduced in 1% HNO<sub>3</sub>. The instrumental mass bias was corrected by exponential law and standard-sample bracketing using the NIST SRM 980 magnesium metal standard that was calibrated against the DSM-3 Mg isotope standard (Galy et al., 2003). Each standard and sample measurement consisted of a cycle of two blocks of 30 measurements (integration time of 10 seconds) with a concentration of 500 ng g<sup>-1</sup>, corresponding to 22 V for 10<sup>11</sup>  $\Omega$  amplifiers on  $^{24}\text{Mg}$ . Reproducibility and accuracy were checked over the course of analyses by repeated measurements of the synthetic standard Cambridge 1 (Galy et al., 2003) and the USGS BCR-2 standard. All

the ratios are expressed in ‰, where x stands for  $^{25}\text{Mg}$  or  $^{26}\text{Mg}$ , following:

$$\delta^x\text{Mg} = \left[ \left( \frac{\left( \frac{x\text{Mg}}{^{24}\text{Mg}} \right)_{\text{sample}}}{\left( \frac{x\text{Mg}}{^{24}\text{Mg}} \right)_{\text{SRM 980}}} \right) - 1 \right] * 10^3 \quad (1)$$

The excess in  $^{26}\text{Mg}$  ( $\delta^{26}\text{Mg}^*$ ) was calculated using a beta factor of 0.511, and each measurement is the average of ~14–22 individual measurements. All uncertainties reported are 2SE uncertainties. The  $\delta^{26}\text{Mg}^*$  calculated for the BCR-2 terrestrial standard was  $0.021 \pm 0.010$  ‰ (n = 42).

The  $(^{26}\text{Al}/^{27}\text{Al})_0$  and  $\delta^{26}\text{Mg}^*_0$  were calculated from the isochron regression fitted using the IsoPlot software (Vermeesch, 2018). The  $^{26}\text{Al}$ - $^{26}\text{Mg}$  relative age was calculated using the canonical  $^{26}\text{Al}/^{27}\text{Al}$  ( $5.23 \times 10^{-5}$ ; Jacobsen et al., 2008) and a  $^{26}\text{Al}$  half-life of 0.717 Ma (Basunia and Hurst, 2016).

## 2.9 Noble gas mass spectrometry

### 2.9.1 Ne isotopes

Analyses of the abundance and isotopic composition of neon contained in one 5.4 mg-sized bulk sample of Néma 001 were performed on the noble gas analytical platform at Institut de Physique du Globe de Paris. Noble gases were extracted in three heating steps using a diode laser (1064 nm, Laser 2000). After extraction, reactive chemical species were sequentially purified using three getters. All noble gases were then trapped on a stainless-steel trap held at a low temperature (< 10 K) using a cryogenic stage. The trap was then heated to 25 K in order to release neon in the gas phase. Neon was then admitted into a Noblesse noble gas mass spectrometer (HR 3F6M version, Nu Instruments) for detection of neon isotopes in multi-collection on electron multipliers. Potential signal interferences from  $^{40}\text{Ar}^{++}$  and  $\text{CO}_2^{++}$  were corrected by measuring  $^{40}\text{Ar}^+$  and  $\text{CO}_2^+$  signals by peak jumping and applying a correction factor using a double ionization ratio, although corrections represent less than 1% of the measured signal. Additional details about the analytical procedure can be found in Avice et al. (2023) and Cattani et al. (2024). Results are reported in Table S9 (Tartèse et al., 2025). Note that we also analysed Ar, Kr, and Xe but the signals were too low compared to the blank signals, which is why we only report Ne isotope results.

### 2.9.2 Ar isotopes

$^{40}\text{Ar}$ - $^{39}\text{Ar}$  age determinations were performed at the University of Manchester using stepped laser heating of two plagioclase separates (1.4 and 1.12 mg) identified from a crushed bulk sample and picked using optical microscopy. Aliquots of Hb3gr monitor ( $1081.0 \pm 1.2$  Ma; Renne et al., 2011) were positioned in close proximity (few mm) to the samples in silica glass vials for irradiation at the Missouri University Research Reactor (USA). The J value, a parameter that is representative of the neutron irradiation conditions, was  $0.003446016 \pm 0.000011359$  (1 $\sigma$ , including



**Figure 1.** Néma 001 hand specimen photographs. Left shows the main sample mass with a partial black shiny fusion crust. Right shows the cut meteorite surface. The green minerals are clinopyroxene, white minerals are plagioclase.

uncertainties on Hb3gr measurements and the uncertainty on the monitor age).

Stepped heating was performed using a Photon Machines Fusions IR 10.6  $\mu\text{m}$  wavelength  $\text{CO}_2$  laser coupled to a Thermo Scientific™ Argus VI preparation bench and multi-collector mass spectrometer. The sample was lased using a 3 mm defocused beam for 30 s with increasing watt output power at each step until the sample was degassed. The released gas was cleaned for two minutes on a hot getter, and then one minute on a hot and cold getter prior to introduction to the mass spectrometer. Isotopes  $^{40}\text{Ar}$ ,  $^{38}\text{Ar}$ , and  $^{37}\text{Ar}$  were measured on Faraday cups, and  $^{39}\text{Ar}$  and  $^{36}\text{Ar}$  on a *Compact Discrete Dynode* (CCD) detector (except for  $^{36}\text{Ar}$  in the plagioclase 1.12 mg split that was measured on a Faraday cup). Data have been corrected for blank contribution (average of session-derived blanks), mass discrimination, neutron-induced interference isotope production on  $^{40}\text{Ar}$ ,  $^{39}\text{Ar}$ ,  $^{38}\text{Ar}$ , and  $^{36}\text{Ar}$ , and decay of  $^{37}\text{Ar}$  and  $^{39}\text{Ar}$  since irradiation.  $^{40}\text{Ar}$ - $^{39}\text{Ar}$  dates were calculated using the decay constant  $\lambda^{40}\text{K}_{\text{total}} = 5.5305(\pm 0.0132) \times 10^{-10} \text{ a}^{-1}$  (Renne et al., 2011). These dates are reported with their two standard deviation ( $2\sigma$ ) level of uncertainty; plateau and isochron dates were calculated using IsoplotR v6.5 (Vermeesch, 2018). All Ar isotope data are reported in Table S10 (Tartèse et al., 2025).

Cosmogenic exposure ages were calculated using two approaches described below.

**Isotope ratio age** This is a mass independent approach that uses the ratio of cosmogenic  $^{38}\text{Ar}_c$  (from the relationship  $^{38}\text{Ar}_c = (5.35 \times ^{38}\text{Ar} - ^{36}\text{Ar}) / (5.35 - 0.65)$ ; where 5.35 is the trapped  $^{36}\text{Ar}/^{38}\text{Ar}$  solar wind ratio and 0.65 is the trapped  $^{36}\text{Ar}/^{38}\text{Ar}$  cosmogenic ratio of Hennessy and Turner, 1980) to the concentration of  $^{37}\text{Ar}$  derived from the measured Ar isotope molar ratios.  $^{38}\text{Ar}_c/^{37}\text{Ar}$  ratios then provide apparent cosmic ray exposure (CRE) ages using P38  $4\pi$

cosmogenic production rates of Eugster and Michel (1995) following the method of Lindsay et al. (2014). CRE ages are reported with their  $2\sigma$  uncertainties, which include a 10% uncertainty on the  $^{38}\text{Ar}$  production function.

**Conventional T38 age** Calculated using the ratio of cosmogenic  $^{38}\text{Ar}_c$  (as calculated above) to the sample mass. The  $^{38}\text{Ar}_c/\text{mass}$  ratios then provide apparent cosmic ray exposure (CRE) ages using the Néma 001 plagioclase average chemical composition determined by EPMA and P38  $4\pi$  cosmogenic production rates of Eugster and Michel (1995). This follows the method of Lindsay et al. (2014), but also considers K, Fe, Ti, Cr, and Mn as target elements in the plagioclase. CRE ages are reported with their  $2\sigma$  uncertainties, which include a 10% uncertainty on the  $^{38}\text{Ar}$  production function and an assumed 10% analytical uncertainty on the reported sample composition.

### 3 Results

#### 3.1 Mineralogy and mineral chemistry

Néma 001 is a coarse-grained igneous rock partly covered by a thin black shiny fusion crust (Figure 1). It comprises a single 68.1 g stone, together with a few fragments found in the immediate vicinity amounting to 7.7 g.

It has a subophitic texture and is composed primarily of mm- to cm-sized crystals of plagioclase (63.8 vol%), olivine (14.6 vol%), orthopyroxene (10.0 vol%), and clinopyroxene (11.4 vol%), with accessory apatite, ilmenite, chromite, kamacite, and troilite (mineral modal abundance determined by X-ray imaging of 5 polished surfaces representing a surface area of 13.1  $\text{cm}^2$ ; e.g., Figure 2). Note that because of the large grain size of most major minerals (Figures 1 and 2), calculated modal abundances may not be entirely representative of Néma 001's parent lithology.



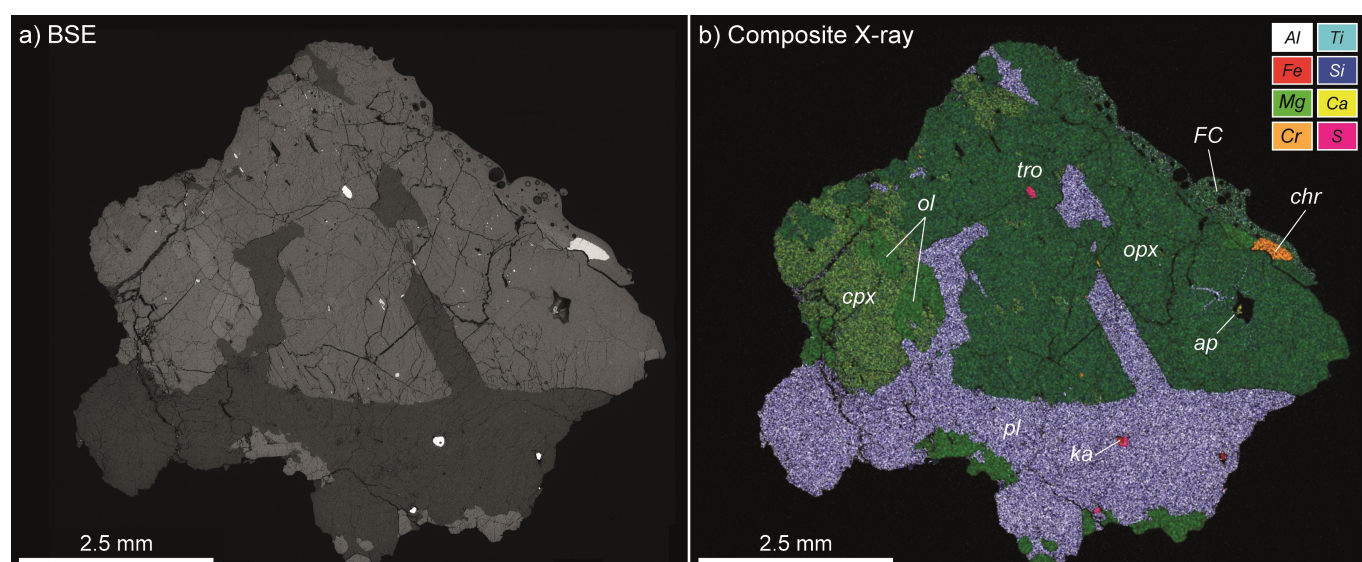


**Figure 2.** Back-scattered electron (BSE) image (a) and composite X-ray map (b) of one of the studied sections of Néma 001. Abbreviations are ap = apatite, chr = chromite, cpx = clinopyroxene, ka = kamacite, ol = olivine, opx = orthopyroxene, pl = plagioclase, tro = troilite, FC = fusion crust.

The major minerals have homogeneous chemical compositions, with albitic plagioclase at  $An_{7.7 \pm 0.9}Ab_{86.5 \pm 0.4}Or_{5.8 \pm 0.6}$ , olivine at  $Fa_{23.2 \pm 0.3}$ , orthopyroxene at  $Fs_{19.7 \pm 0.5}Wo_{1.8 \pm 0.4}$ , and clinopyroxene at  $Fs_{7.5 \pm 0.5}Wo_{44.8 \pm 1.6}$  (Figure 3 and Tables S2 and S11, Tartèse et al., 2025). Molar Fe/Mn ratios of olivine, orthopyroxene, and clinopyroxene are  $24.6 \pm 1.3$  (1SD,  $n = 18$ ),  $15.1 \pm 0.6$  (1SD,  $n = 6$ ), and  $10.7 \pm 1.4$  (1SD,  $n = 7$ ), respectively (Table S2, Tartèse et al., 2025). Chromite is also homogeneous, with a composition of  $Chr_{79.8}Ulv_{14.5}Sp_{5.7}$ , and contains 0.43 wt%  $V_2O_3$  and 0.13 wt% ZnO (Table S2, Tartèse et al., 2025). It contains less Fe than chromite in ordinary chondrites, and plot just outside the acapulcoite-lodranite field in a  $Cr/(Cr+Al)$  vs.  $Fe/(Fe+Mg)$  diagram (Figure 3d). Olivine in Néma 001 is less magnesian than in acapulcoites-lodranites (Figure 3b), and plagioclase is more albitic than in acapulcoites-lodranites (Figure 3c). In general, pyroxene in Néma 001 are more magnesian than in other differentiated achondrites (Figure 3a). On the other hand, pyroxenes in Néma 001 are more ferroan than in acapulcoites, lodranites, and gabbroic clasts in transitional acapulcoite LEW 86220 (Figure 3a). Plagioclase in Néma 001 also tends to be more albitic than in other differentiated ungrouped achondrites (Figure 3c).

Trace element abundances are also relatively homogeneous among the various mineral phases, as shown by mineral rare earth element (REE) abundances (Figure 4). Apatite contains the highest REE abundances, followed by clinopyroxene; plagioclase displays large positive Eu-anomalies, and all other minerals displays negative Eu-anomalies (Figure 4). Clinopyroxene in Néma 001 has slightly lower light REE and higher heavy REE abundances than clinopyroxene in gabbroic clasts in LEW 86220 (Figure 4), which have been interpreted as partial melting products of lodranite precursor (Lucas et al., 2022). Orthopyroxene in Néma 001 has similar middle REE and higher heavy REE abundances than orthopyroxene in LEW 86220 gabbro (Figure 4).

The chemical compositions of the two pyroxenes can be used to estimate equilibration temperatures. Using the major element abundances of orthopyroxene and clinopyroxene (Table S11, Tartèse et al., 2025) and the thermometer of Brey and Köhler (1990) yields a temperature of 916 °C (for a pressure fixed at 20 MPa that would correspond to a depth of ~50 km for an asteroid with a rock density of 3800 kg m<sup>-3</sup> and a gravitational acceleration  $g$  of 0.1 m s<sup>-2</sup>; the dependency on pressure is small as calculated temperatures range between 915 and 919 °C for pressures of 0.4 MPa (~1 km depth) and 190 MPa (~500 km depth). The REE-in-two-pyroxene thermometer of Liang et al. (2013) yields a temperature of  $904 \pm 5$  °C for orthopyroxene-clinopyroxene pairs in Néma 001. The temperatures derived using these two thermometers are remarkably consistent with one another, and likely record subsolidus pyroxene closure temperatures.

## 3.2 Bulk rock composition

### 3.2.1 Oxygen isotopes

Bulk oxygen isotope analyses of Néma 001 yielded  $\delta^{17}O = 0.62 \pm 0.08\text{‰}$  and  $\delta^{18}O = 3.26 \pm 0.12\text{‰}$ , corresponding to a  $\Delta^{17}O$  value of  $-1.07 \pm 0.03\text{‰}$  (representing the vertical deviation from the terrestrial fractionation line, assumed to have a slope of 0.52 in  $\delta^{17}O$  vs.  $\delta^{18}O$  space). These O isotope characteristics are similar with those of most acapulcoites and lodranites (Figure 5a), consistent with derivation of Néma 001 from the acapulcoite-lodranite asteroidal parent body. We note that the relatively small powdered aliquot (~7 mg) used for O isotope analyses may not be fully representative of the bulk mineralogy of Néma 001 in view of the large mineral grain size; however, for a given planetary body  $\Delta^{17}O$  values are identical among various mineral phases, and the maximum  $\delta^{18}O$  fractionation between the main silicate minerals is about 1‰ at magmatic temperatures relevant to achondrites (e.g., Clayton, 1993).

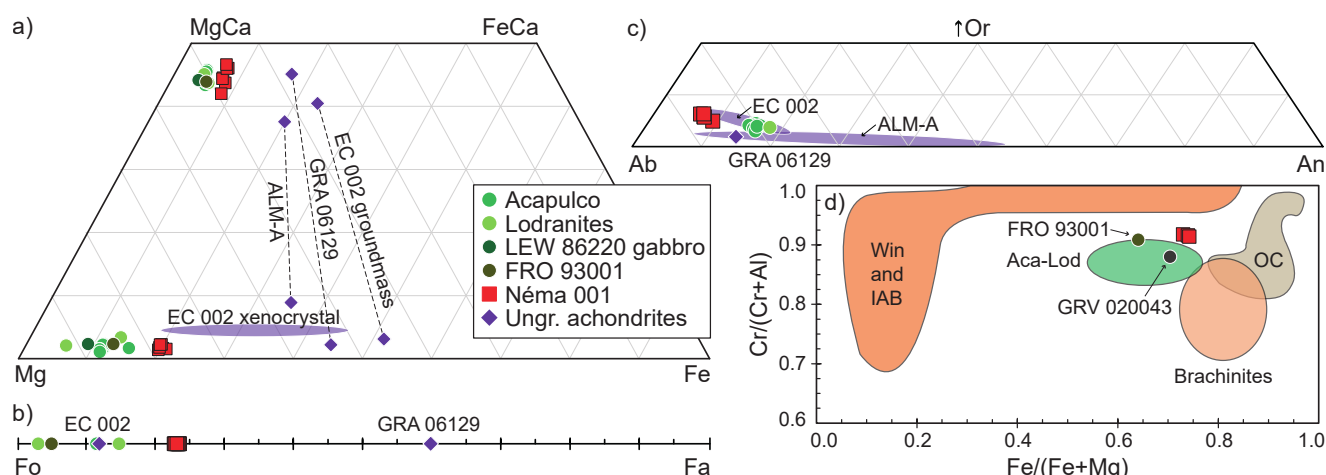


**Figure 3.** Chemical composition of pyroxene (a), olivine (b), plagioclase (c), and chromite (d) in Néma 001. For (a–c) the composition of Néma 001 silicates is compared to that of those minerals in Acapulco (Dhaliwal et al., 2017), gabbro clasts in acapulcoite LEW 86220 (Lucas et al., 2022), FRO 93001 (Folco et al., 2006), the lodranites Lodran and Gibson (McCoy et al., 1997a; Takeda et al., 1994), and the andesitic/trachyandesitic ungrouped achondrites GRA 06129 (Shearer et al., 2010), ALM-A (Bischoff et al., 2014), and Erg Chech 002 (EC 002; Barrat et al., 2021). In (d), the composition of chromite in Néma 001 is compared to that of a range of meteorite groups – see Folco et al. (2006) and Li et al. (2018) for literature data sources.

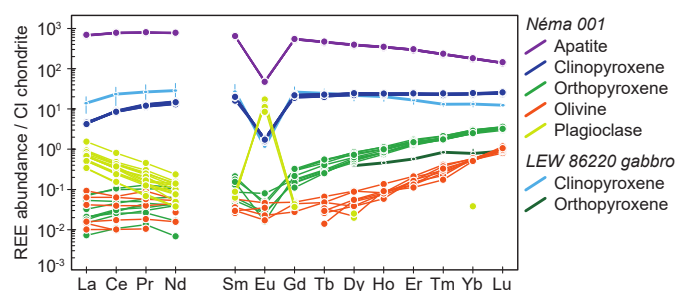


**Figure 4.** CI chondrite-normalised REE abundances for minerals in Néma 001. The diagram also displays the REE abundance of orthopyroxene and clinopyroxene in gabbro clasts in acapulcoite LEW 86220 (Lucas et al., 2022). The CI chondrite composition used for normalising is from Barrat et al. (2012).

Therefore, even allowing for small variations of  $\delta^{18}\text{O}$  values would not change our interpretation of O isotope data. In contrast to the similarity between Néma 001 and the acapulcoites and lodranites, most other known achondrites have different bulk oxygen isotope compositions compared to Néma 001. The ungrouped achondrites Northwest Africa (NWA) 6693/6704/10132, which are likely paired (Greenwood et al., 2017), have similar  $\Delta^{17}\text{O}$  values to Néma 001 with slightly higher  $\delta^{18}\text{O}$  values (Figure 5a). However,  $\varepsilon^{54}\text{Cr}$  and  $\varepsilon^{50}\text{Ti}$  isotope anomalies show that these meteorites are carbonaceous achondrites that cannot be related to the acapulcoites-lodranites (e.g., Sanborn et al., 2019).

### 3.2.2 Major and minor elements

We combined the modal mineralogy and average mineral compositions to calculate a bulk major and trace element composition for Néma 001 (Table S11, Tartèse et al., 2025).

In a total alkalis ( $\text{Na}_2\text{O} + \text{K}_2\text{O}$ ) vs. silica (TAS) diagram, Néma 001 plots between the andesite and trachyandesite fields, similarly to other ungrouped achondrites such as Grave Nunataks (GRA) 06128/06129 (Day et al., 2009, 2012; Shearer et al., 2010), Erg Chech 002 (Barrat et al., 2021), and the evolved clast ALM-A from the Almahata Sitta polymict meteorite (Bischoff et al., 2014) (Figure 5b).

Figure 6 depicts some of the bulk major element abundances reconstructed from modal mineral abundances and their chemical compositions (Table S11, Tartèse et al., 2025), together with the composition of liquids produced by partial melting of a range of ordinary chondrites (OC) at 1050–1350 °C and  $f\text{O}_2$  between IW-2.4 and IW+0.8 (Jurewicz et al., 1995; Feldstein et al., 2001; Usui et al., 2015; Collinet and Grove, 2020b). It also includes the average composition of melts extracted from the lodranite parent body calculated by Collinet and Grove (2020a), and the compositions of liquids formed by partial melting of a source with the composition of the type 4 chondrite GRV 020043 (using modal mineralogy and mineral compositions from Li et al., 2018) calculated using rhyolite-MELTS\_v1.0.x (Gualda et al., 2012) for temperatures ranging between 1050 and 1600 °C, a pressure of 20 MPa, and  $f\text{O}_2$  of IW-2 (see Table S12, Tartèse et al., 2025, for full results).

The calculated bulk composition of Néma 001 (58.3 wt%  $\text{SiO}_2$ , 12.1 wt%  $\text{Al}_2\text{O}_3$ , 6.0 wt%  $\text{FeO}$ , 12.7 wt%  $\text{MgO}$ , 4.1 wt%  $\text{CaO}$ , 5.7 wt%  $\text{Na}_2\text{O}$ ; Table S11, Tartèse et al., 2025) appears enriched in  $\text{MgO}$  and depleted in  $\text{FeO}$  and  $\text{CaO}$  for its  $\text{SiO}_2$  abundance compared to the composition of OC experimental partial melts (Figure 6), which largely reflects the large modal abundance of olivine (~15 vol%). Reaching such bulk  $\text{MgO}$  abundances typically requires temperatures of ca. 1300 °C for OC partial melts (Jurewicz et al., 1995; Usui et al., 2015; Collinet and Grove, 2020b).



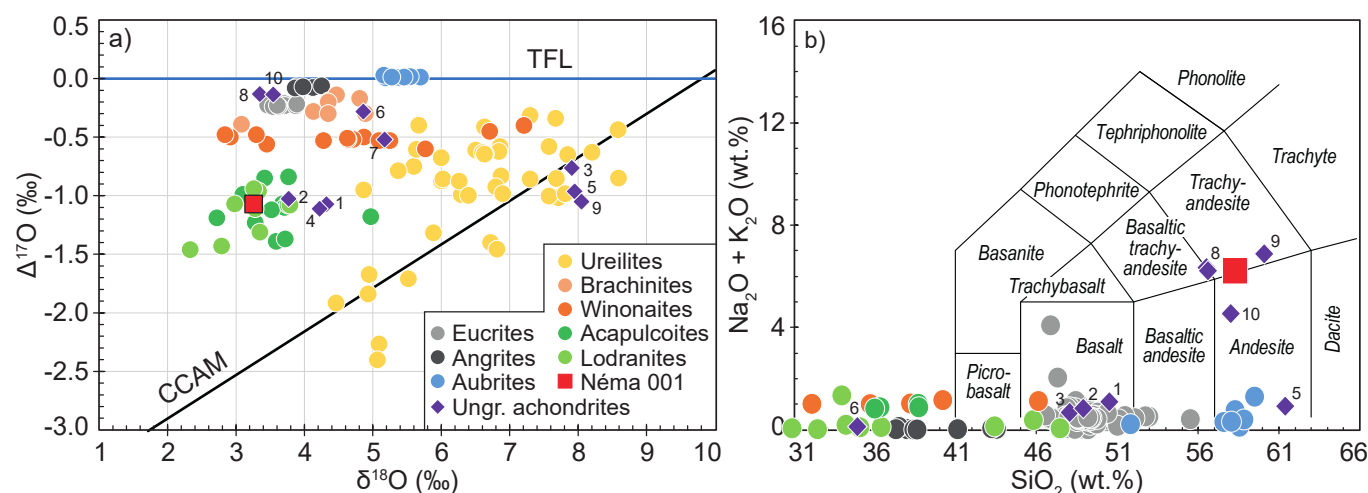


**Figure 5.** Some geochemical characteristics of Néma 001. a) Triple oxygen isotope composition of Néma 001 compared to other achondrite meteorites (TFL and CCAM stand for Terrestrial Fractionation Line and Carbonaceous Chondrite Anhydrous Mineral, respectively); b) Total bulk rock alkali ( $\text{Na}_2\text{O} + \text{K}_2\text{O}$ ) vs.  $\text{SiO}_2$  diagram, depicting the composition of Néma 001 compared to other achondrite meteorites. Bulk rock oxygen isotope data can be found in Greenwood et al. (2012, 2017), Bischoff et al. (2014), and in the Meteorite Bulletin (<https://www.lpi.usra.edu/meteor/>) for ungrouped achondrites NWA 6693 (1), 6704 (2), 7325 (3), 10132 (4), 11119 (5), Divnoe (6), Dhofar 732 (7), GRA 06128 (8), ALM-A (9), and Erg Chech 002 (10); bulk rock major element compositions can be found in Keil (2012) for angrites, in Easton (1985) for aubrites, in Mittlefehldt (2015) for basaltic eucrites, in Hunt et al. (2017) for winonaites, in Keil and McCoy (2018) for acapulcoites and lodranites, and in Petaev et al. (1994), Day et al. (2009, 2012), Shearer et al. (2010), Warren et al. (2013), Bischoff et al. (2014), Barrat et al. (2015, 2021), Srinivasan et al. (2018), and Hibiya et al. (2019) for ungrouped achondrites.

Considering that olivine is one of the most refractory phase during partial melting of a chondritic lithology, this may suggest that olivine in Néma 001 is a xenocristic restite phase entrained in the melt. This would be consistent with its typical size of ca. 500–750  $\mu\text{m}$  (Figure 1), which is similar to olivine size in lodranites that have experienced 5 to >10% partial melting (McCoy et al., 1997b). With this assumption, Figure 6 also displays some of the major element abundances for an olivine-free calculated Néma 001 composition; this composition (62.7 wt%  $\text{SiO}_2$ , 14.7 wt%  $\text{Al}_2\text{O}_3$ , 2.6 wt%  $\text{FeO}$ , 6.8 wt%  $\text{MgO}$ , 5.0 wt%  $\text{CaO}$ , 6.9 wt%  $\text{Na}_2\text{O}$ ; Table S11 Tartèse et al., 2025) matches reasonably well with that of some partial melts obtained during melting of OC at ca. 1150–1200 °C (Figure 6) and with the average composition of melts extracted from the lodranite parent body calculated by Collinet and Grove (2020a). Except for the  $\text{CaO}$  abundance, the melt compositions obtained for partial melting of GRV 020043 at ca. 1150–1200 °C using rhyolite-MELTS are also similar to the olivine-free Néma 001 major element composition (Figure 6).

### 3.2.3 Trace elements

The bulk trace element composition calculated from modal mineralogy and average mineral compositions and that measured by solution ICP-MS on sawing dust are consistent, except for elements such as Cr, Ni, Co, Cu, Nb, and Pb whose abundances are much higher in the sawing dust (Table S11, Tartèse et al., 2025). This likely result from a combination of contamination from the saw wire and omission of a few accessory phases in the modal recombination in which

these elements are abundant such as chromite and Fe-metal. On the other hand, the remarkable consistency for the other elements suggest that our modal mineralogy estimate is fairly representative of the bulk of Néma 001. Based on the discussion above, we focus here on the calculated olivine-free composition of Néma 001.

Most trace element abundances in Néma 001 are between 1 and 10 times CI chondrite abundances (Figure 7a), although Néma 001 contains very little Cu ( $\sim 1 \mu\text{g.g}^{-1}$ ) and Pb ( $\sim 6 \text{ ng.g}^{-1}$ ). Incompatible trace element abundances (e.g., REE, Th, U) are about 5–8 times the CI chondrite abundances. The CI-normalised REE pattern of Néma 001 is flat, showing slight light REE depletion ( $\text{La}_n/\text{Sm}_n = 0.76$ ) and a small positive Eu anomaly ( $\text{Eu}/\text{Eu}^* = 1.17$ ). Compared to other andesitic achondrites, Néma 001 REE abundances are similar to those in Erg Chech 002 and NWA 11119, with slightly higher light REE abundances; abundances for the large-ion lithophile elements Sr, Cs, Ba, and Eu are similar to those in Erg Chech 002, with significant enrichments in volatile incompatible elements such as K and Rb in Néma 001 (Figure 7a). In fact, Néma 001's K/Th ratio of ca. 63000 is about 3 times higher than in CI chondrites (ca. 19400; Barrat et al., 2012). On the other hand, Néma 001 appears significantly depleted in Nb, and to a lesser extent Li, compared to other andesitic achondrites (Figure 7a). Except for K and to a lesser extent Zr abundances, the trace element composition of Néma 001 matches well with that of silicate melts produced by 10–15% disequilibrium partial melting of an OC starting composition over a week (Feldstein et al., 2001, Figure 7b).

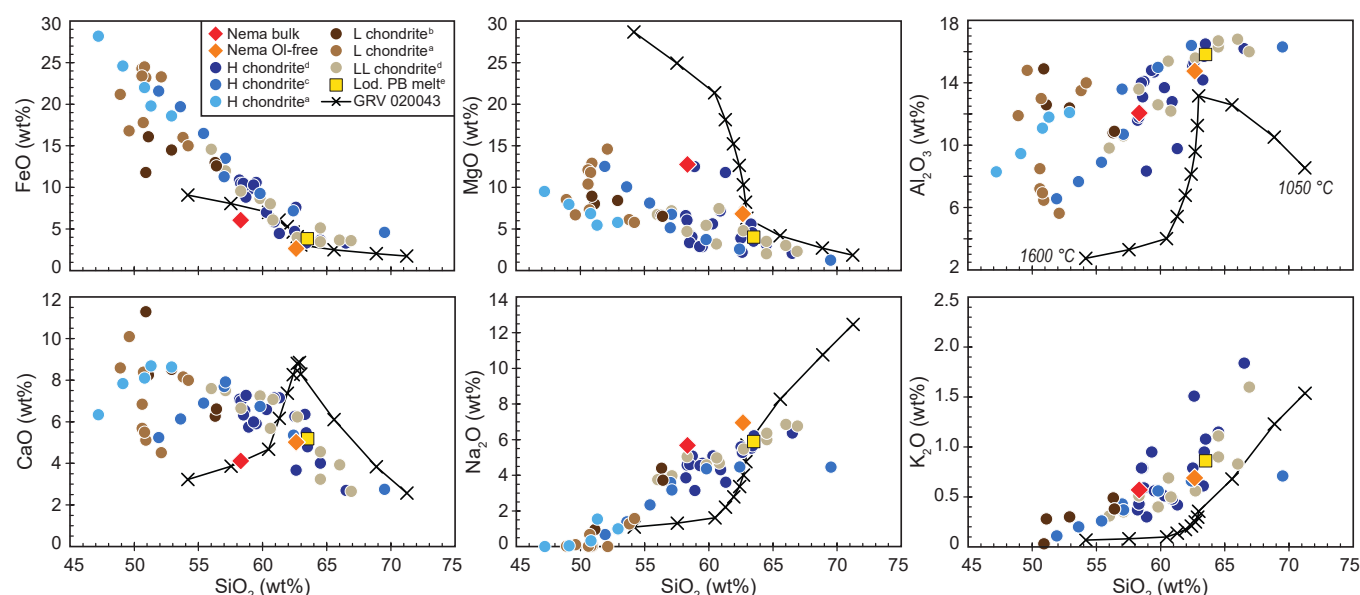


**Figure 6.** Calculated bulk rock major element compositions of Néma 001 and olivine-free Néma 001 (see text for details). These are compared to the compositions of liquids produced by partial melting of a range of ordinary chondrites at 1050–1350 °C and  $fO_2$  between IW-2.4 and IW+0.8 (Jurewicz et al. 1995 (a); Feldstein et al. 2001 (b); Usui et al. 2015 (c); Collinet and Grove 2020b (d)), the average calculated composition of melts extracted from the lodranite parent body of Collinet and Grove (2020a) (e), and the compositions of liquids formed by partial melting of a source with the composition of the type 4 chondrite GRV 020043 (from Li et al., 2018, see text for details) calculated using rhyolite-MELTS\_v1.0.x for temperatures ranging between 1050 and 1600 °C, a pressure of 20 MPa, and  $fO_2$  of IW-2 (crosses denote 50 °C melting increments).

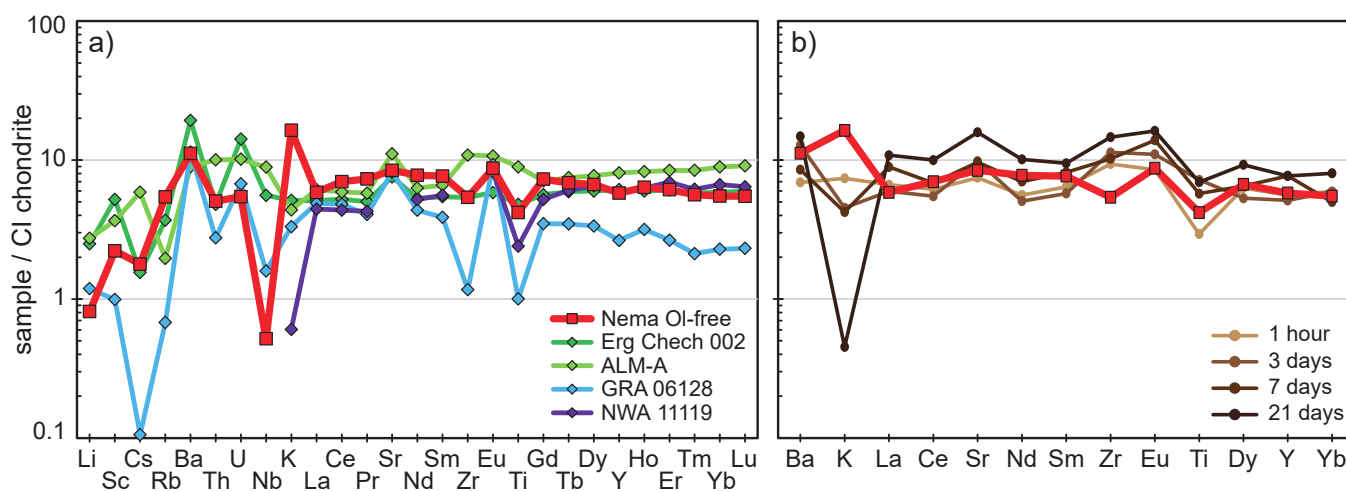


**Figure 7.** CI chondrite-normalised trace element abundances in the olivine-free Néma 001 calculated bulk composition compared to (a) those of the other andesitic achondrites Erg Chech 002 (Barrat et al., 2021), the evolved clast ALM-A from the Almahata Sitta polymict meteorite (Bischoff et al., 2014), GRA 06128 (Day et al., 2009), and NWA 11119 (Srinivasan et al., 2018), and (b) those of experimental melts produced over 3 weeks by disequilibrium melting of the L6 ordinary chondrite Leedey (Feldstein et al., 2001).

### 3.3 Geochronology

#### 3.3.1 Al/Mg dating

The internal isochron obtained on the bulk rock and mineral separate fractions yielded an initial  $\delta^{26}\text{Mg}^*_0$  of  $0.011 \pm 0.007\text{‰}$  and a slope corresponding to a  $(^{26}\text{Al}/^{27}\text{Al})_0$  ratio of  $2.17(\pm 0.32) \times 10^{-6}$  ( $2\sigma$ ,  $n = 4$ , MSWD = 2.6; Figure 8), which translates to a closure date of the  $^{26}\text{Al}$ - $^{26}\text{Mg}$  system

of  $3.29 \pm 0.17$  Ma after the formation of CAIs, assuming a canonical distribution of  $^{26}\text{Al}$  in the protoplanetary disk (Jacobsen et al., 2008; Villeneuve et al., 2009). The  $^{27}\text{Al}/^{24}\text{Mg}$  ratios of the plagioclase fraction is 6.1 (Table S8, Tartèse et al., 2025), which is much lower than the  $^{27}\text{Al}/^{24}\text{Mg}$  ratio of pure plagioclase as LA-ICP-MS analyses typically yielded  $^{27}\text{Al}/^{24}\text{Mg}$  of  $\sim 4000$ – $5000$  for Néma 001 plagioclase. This suggests that the plagioclase fraction ( $\sim 106000 \mu\text{g.g}^{-1}$  Al

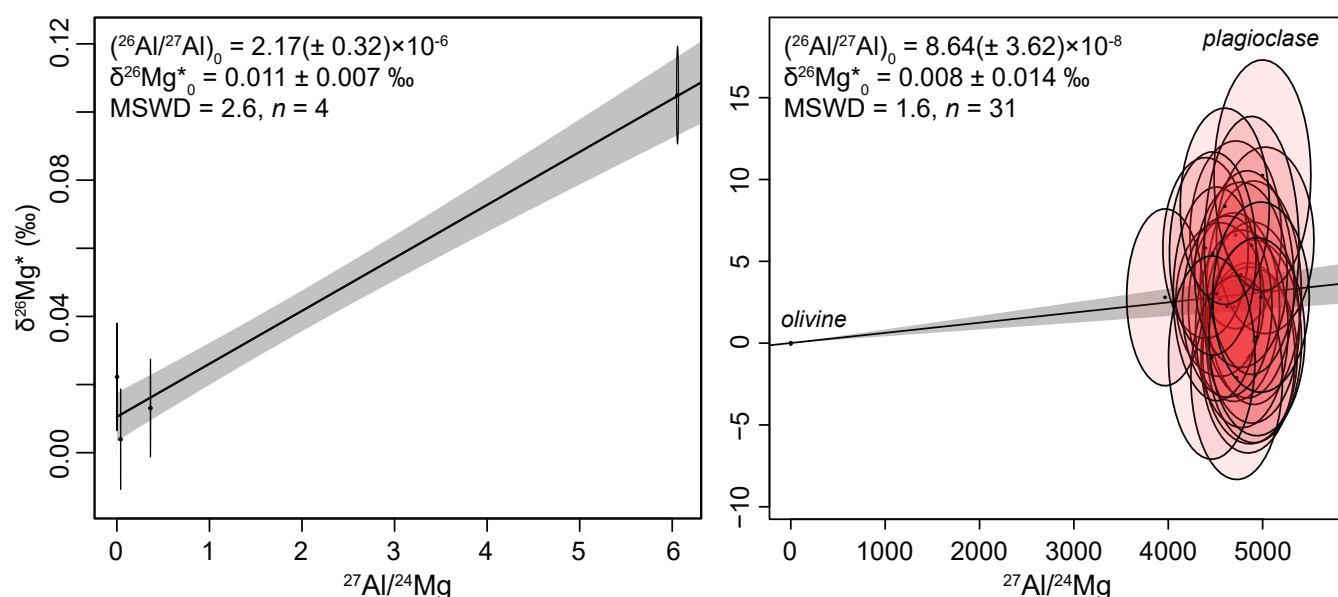


**Figure 8.** Internal Al/Mg isochrons obtained for Néma 001 by wet chemistry on bulk rock and mineral separate fractions (left) and in situ by SIMS on olivine and plagioclase (right). The bulk + mineral isochron corresponds to a date of  $3.29 \pm 0.17$  Ma after CAI and the olivine-plagioclase in situ isochron corresponds to a date of  $6.6 \pm 0.6$  Ma after CAIs.

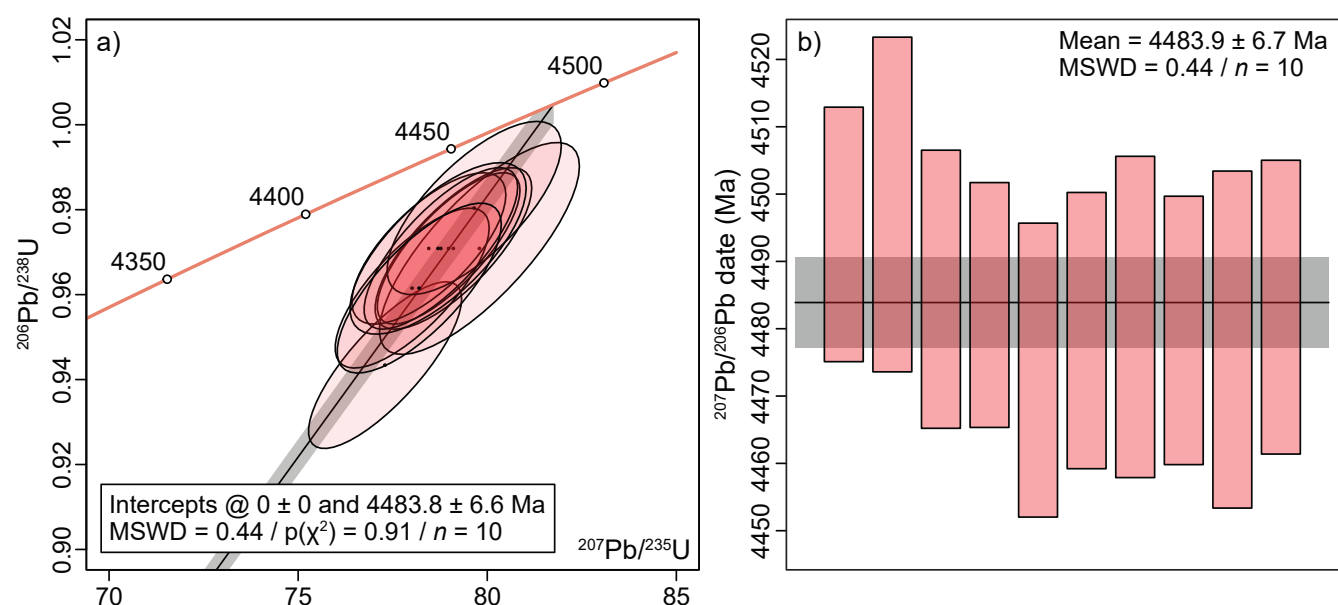


**Figure 9.** Apatite U-Pb dating. Data are plotted in a conventional Wetherill diagram (a) and as weighted average  $^{207}\text{Pb}/^{206}\text{Pb}$  date (b).

and  $50 \mu\text{g.g}^{-1}$  Mg for pure plagioclase) included some Mg-rich phases, indeed contamination by  $\sim 10\%$  ferromagnesian phases ( $\sim 1100 \mu\text{g.g}^{-1}$  Al and  $180000 \mu\text{g.g}^{-1}$  Mg, using modal abundances of olivine, orthopyroxene, and clinopyroxene) would decrease the  $^{27}\text{Al}/^{24}\text{Mg}$  ratio to  $\sim 6$ – $7$ . This isochron, thus, largely reflects closure of the Al/Mg system in ferromagnesian silicates.

In situ SIMS analyses of olivine and plagioclase in Néma 001 yielded  $^{27}\text{Al}/^{24}\text{Mg}$  ratios of  $0.6$ – $4 \times 10^{-4}$  and  $3967$ – $5027$ , respectively, associated with weighted average  $\delta^{26}\text{Mg}^*$  value of  $0.003 \pm 0.020$  ‰ for olivine (95% confidence,  $n = 8$ , MSWD = 2.8) and  $2.9 \pm 1.3$  ‰ for plagioclase (95% confidence,  $n = 24$ , MSWD = 1.6) (Table S8, Tartèse

et al., 2025). These limited  $^{26}\text{Mg}$  enrichments in Néma 001 plagioclase obtained by SIMS indicate that it closed below the Mg diffusion temperature when most  $^{26}\text{Al}$  had decayed. This is reflected by an olivine-plagioclase isochron that yields an initial  $(^{26}\text{Al}/^{27}\text{Al})_0$  ratio of  $8.6(\pm 3.6) \times 10^{-8}$  ( $2\sigma$ ,  $n = 31$ , MSWD = 1.6; Figure 8), which corresponds to a closure date of the  $^{26}\text{Al}$ – $^{26}\text{Mg}$  system in plagioclase of  $6.6 \pm 0.6$  Ma after the formation of CAIs, assuming a canonical distribution of  $^{26}\text{Al}$  in the protoplanetary disk (Jacobsen et al., 2008; Villeneuve et al., 2009). The regression yielded a  $\delta^{26}\text{Mg}^*_0$  of  $0.008 \pm 0.014$  ‰, identical to the value determined on bulk and mineral fractions.



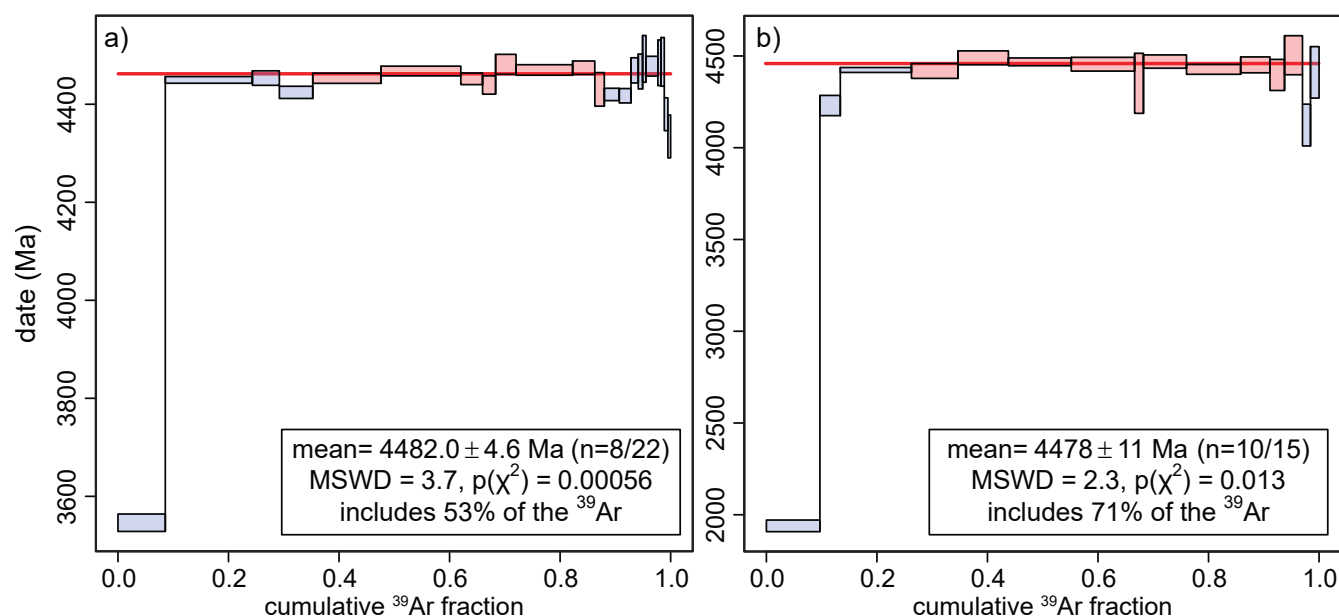


**Figure 10.**  $^{40}\text{Ar}/^{39}\text{Ar}$  date release spectra for the plagioclase splits 1 (a) and 2 (b) and calculated apparent plateau dates. Steps in light blue are excluded for plateau date calculations. Note differences in y-axis scale.

### 3.3.2 Apatite U-Pb dating

We carried out 10 analyses in a large  $\sim\text{mm}$ -sized apatite grain that yielded  $5.9 \pm 0.2 \mu\text{g.g}^{-1}$  U and  $17.0 \pm 1.0 \mu\text{g.g}^{-1}$  Th (Table S6, Tartèse et al., 2025). In a conventional concordia diagram, the apatite  $^{207}\text{Pb}/^{235}\text{U}$  vs.  $^{206}\text{Pb}/^{238}\text{U}$  ratios are slightly discordant, and yield an upper intercept date of  $4484 \pm 7$  Ma when plotted on a discordia anchored to 0 ( $2\sigma$ ,  $n = 10$ , MSWD = 0.4; Figure 9) that is identical to the calculated weighted mean  $^{207}\text{Pb}/^{206}\text{Pb}$  date (Figure 9). The slight discordance of U-Pb ratios may indicate that apatite suffered some limited recent Pb loss, possibly during the ejection of Néma 001 from its parent body.

### 3.3.3 $^{40}\text{Ar}/^{39}\text{Ar}$ dating

We carried out step-heating Ar isotope analyses on two plagioclase splits (split 1 = 1.4 mg and split 2 = 1.12 mg). These analyses yielded  $1.4 \pm 0.1$  (split 1) and  $2.3 \pm 0.1$  wt% CaO (split 2) and  $0.89 \pm 0.02$  (split 1) and  $0.74 \pm 0.02$  wt%  $\text{K}_2\text{O}$  (split 2), based on the measured  $^{37}\text{Ar}$  and  $^{39}\text{Ar}$  abundances, respectively, which is consistent with EPMA analyses ( $1.6 \pm 0.2$  wt% CaO and  $1.0 \pm 0.1$  wt%  $\text{K}_2\text{O}$ ; Table S11, Tartèse et al., 2025). For both splits, the first heating step yielded young apparent  $^{40}\text{Ar}/^{39}\text{Ar}$  dates, while the rest of the release steps yielded relatively flat  $^{40}\text{Ar}/^{39}\text{Ar}$  date spectra, suggesting little gas loss has occurred (Figure 10). These spectra yielded identical  $^{40}\text{Ar}/^{39}\text{Ar}$  apparent plateau dates of  $4482 \pm 5$  Ma (MSWD = 3.7, includes 53% of the  $^{39}\text{Ar}$  released) and  $4478 \pm 11$  Ma (MSWD = 2.3, includes 71% of the  $^{39}\text{Ar}$  released) for splits 1 and 2, respectively (Figure 10). These plateau dates are consistent within errors with dates determined using normal and inverse isochron plots (Supp. Figure 1).

## 3.4 Noble gas inventory and cosmic ray exposure

### 3.4.1 Ne isotopes

The three heating steps yielded Ne isotope ratios clustering close to the cosmogenic composition for average chondrites (Supp. Figure 2), showing that Néma 001 contains very little solar and primordial neon. In detail, the  $^{20}\text{Ne}/^{22}\text{Ne}$  and  $^{21}\text{Ne}/^{22}\text{Ne}$  ratios measured on Néma 001 are slightly lower than those for the cosmogenic component of average chondrites (Supp. Figure 2), which likely reflects the fact that the analysed aliquot contained abundant Na-rich plagioclase that produces a lot of  $^{22}\text{Ne}$ . Using the relationship between bulk chemical composition and cosmogenic  $^{21}\text{Ne}$  production rate (P21) given in Eugster and Michel (1995) yields  $\text{P21} = 2.53 \times 10^{-9} \text{ ccSTP g}^{-1} \text{ Ma}^{-1}$ . In turn this corresponds to a  $^{21}\text{Ne}$  cosmic ray exposure (CRE) age of  $28.5 \pm 5.8$  Ma assuming that all  $^{21}\text{Ne}$  is cosmogenic (uncertainty includes that on the measured  $^{21}\text{Ne}$  abundance and a  $\pm 20\%$  uncertainty on P21; see Wieler et al., 2016). Using the lowest P21 of  $1.4 \times 10^{-9} \text{ ccSTP g}^{-1} \text{ Ma}^{-1}$  of Wieler et al. (2016) for achondrites yields a  $^{21}\text{Ne}$  CRE age of  $51.5 \pm 10.4$  Ma. Considering that the analysed aliquot is dominated by plagioclase, and using the Néma 001 average plagioclase composition determined by EPMA, yields a P21 of  $1.68 \times 10^{-9} \text{ ccSTP g}^{-1} \text{ Ma}^{-1}$ , which in turn corresponds to a  $^{21}\text{Ne}$  CRE age of  $42.8 \pm 8.7$  Ma. Considering these uncertainties, we estimate an imprecise  $^{21}\text{Ne}$  CRE age of  $40 \pm 20$  Ma for Néma 001.

### 3.4.2 Ar isotopes

For both plagioclase splits, the  $^{38}\text{Ar}/^{36}\text{Ar}$  ratios are high and above the cosmogenic ratio of 1.53 (Hennessy and Turner, 1980) for nearly all steps (Supp. Figure 3). This could indicate that there is some contribution of  $^{38}\text{Ar}$  from a Cl-rich phase, as during irradiation  $^{37}\text{Cl}$  converts to

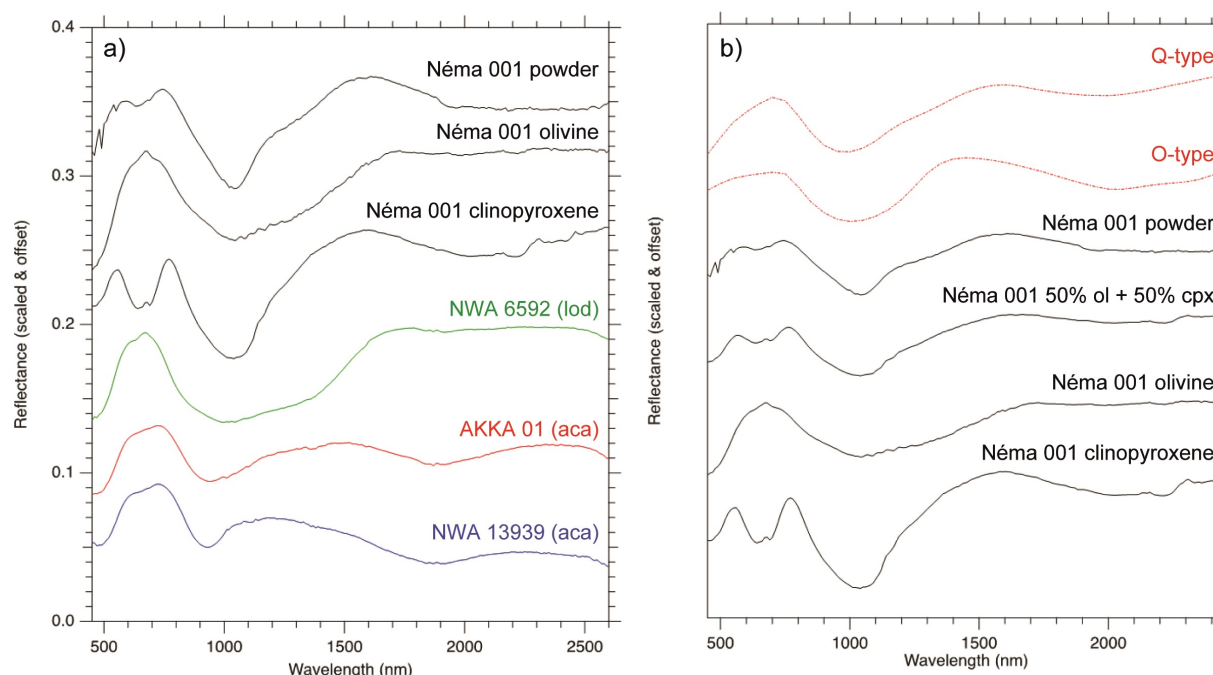


**Figure 11.** a) Reflectance spectra obtained on Néma 001, compared with acapulcoite and lodranite from the RELAB database. The top spectrum was obtained on a powdered sample. The second spectrum from top was obtained in an olivine-rich area and shows the diagnostic signature of olivine that is a broad feature with a maximum of absorption around 1  $\mu\text{m}$ . The third spectra from the top was measured on a green clinopyroxene-rich area and shows the combination of an absorption centred at 1.05  $\mu\text{m}$  and a broad band with a maximum around 2  $\mu\text{m}$ . These two bands and their positions are typical of clinopyroxene. An additional band is observed in the clinopyroxene spectrum with a maximum of absorption around 0.7  $\mu\text{m}$ , possibly due to Cr in the pyroxene that can explain the green colour of this phase. The small positive features around 2.2 and 2.4  $\mu\text{m}$  are artefacts, due to imperfect correction of the resin contribution; b) Reflectance spectra of powdered samples and individual silicate phase of Néma 001, of calculated mixtures of olivine and clinopyroxene, and comparison to asteroidal taxonomic endmembers O and Q defined by DeMeo et al. (2009).

$^{38}\text{Cl}$  due to the capture of a neutron, which will  $\beta$ -decay to  $^{38}\text{Ar}$  with a half-life of 37.3 min. This is similar to what has been observed by Shearer et al. (2010) for 2 bulk splits of the ungrouped achondrite GRA 06129 for which many steps yielded  $^{38}\text{Ar}/^{36}\text{Ar}$  ratios much higher than the cosmogenic ratio, and which they attributed to the presence of Cl-rich apatite. Assuming that all  $^{38}\text{Ar}$  is derived from  $^{38}\text{Cl}$  decay yields bulk Cl abundance of 73 and 105  $\mu\text{g.g}^{-1}$  for the Néma 001 plagioclase splits 1 and 2, respectively (Table S10, Tartèse et al., 2025), which is orders of magnitude higher than the Cl abundances of a few tens of  $\text{ng.g}^{-1}$  measured in plagioclase in acapulcoites and lodranites (Peterson et al., 2024) and the ungrouped achondrite Erg Chech 002 (Peterson et al., 2025), for example. The amounts of  $^{38}\text{Ar}$  produced by  $^{38}\text{Cl}$  decay for Néma 001 plagioclase would require the incorporation of ca. 0.1–0.2 wt% apatite, assuming that apatite in Néma 001 contains  $\sim 5.5$  wt% Cl, similarly to apatite in other andesitic ungrouped achondrites such as GRA 06128/06129 (e.g., Tartèse et al., 2019). When using Ar isotope analyses to calculate CRE ages, the isotope ratio age method yields  $^{38}\text{Ar}$  CRE ages of  $160 \pm 37$  Ma and  $138 \pm 32$  Ma for splits 1 and 2, respectively; the conventional T38 method yields  $^{38}\text{Ar}$  CRE ages of  $115 \pm 30$  Ma and  $165 \pm 49$  Ma for splits 1 and 2, respectively. These CRE ages are higher than our estimated  $^{21}\text{Ne}$  CRE age of  $40 \pm 20$  Ma (see Section 3.4.1),

confirming that they are likely overestimates due to a small amount of Cl-produced  $^{38}\text{Ar}$  contribution.

## 4 Discussion

### 4.1 Petrogenesis of Néma 001

Melts with a broadly andesitic composition such as those represented by the achondrites Néma 001, GRA 06128/06129 (Day et al., 2009, 2012; Shearer et al., 2010), Erg Chech 002 (Barrat et al., 2021), and the evolved clast ALM-A from the Almahata Sitta polymict meteorite (Bischoff et al., 2014, Figure 5b) could in theory derive from more primitive basaltic melts by fractional crystallisation. However, this does not fit with many of their geochemical characteristics such as low incompatible trace element abundances (e.g.,  $\sim 0.14$   $\mu\text{g.g}^{-1}$  Th and REE abundances at  $\sim 6$ –8 times Cl chondrite abundances for Néma 001) and an absence of negative Eu anomaly that would be expected if plagioclase fractionation had taken place (e.g., Barrat et al., 2021). This indicates that Néma 001 likely represents a primary melt, similarly to other andesitic achondrites (e.g., Bischoff et al., 2014; Barrat et al., 2021). Indeed, the bulk composition of Néma 001 is consistent with that of silicate liquids formed by low pressure melting of OC-like lithologies at ca.

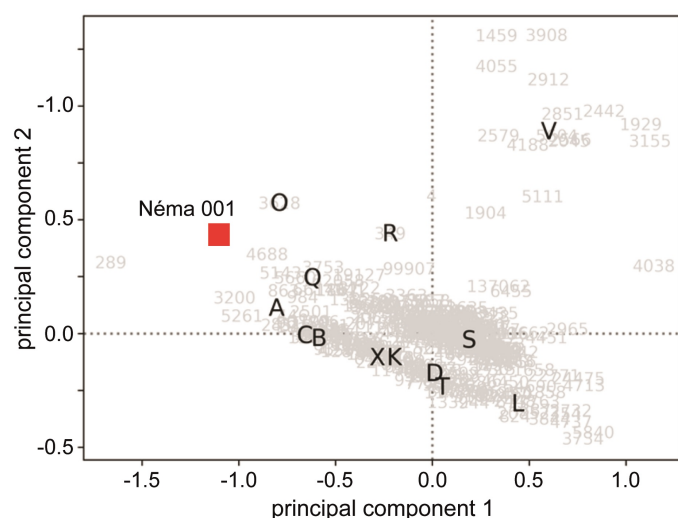


**Figure 12.** Principal components PC1 and PC2 of the taxonomic classification for endmember asteroids (where bold letters denote main asteroid groups) and the Néma 001 olivine-clinopyroxene 50:50 model mixture, using the taxonomy of [Mahlke et al. \(2022\)](#).

1150–1200 °C and  $fO_2$  1–2 log units below the IW buffer (Figure 6).

These experimental studies show that the MgO abundance of silicate liquids formed by ordinary chondrite partial melting is a good proxy to estimate the melting temperature (Supp. Figure 4). Using this empirical relationship yields a temperature of ca.  $1200 \pm 30$  °C for the olivine-free bulk Néma 001 MgO abundance of 6.75 wt%, which is well within the range of lodranite partial melting temperatures of ca. 1100–1250 °C ([Mittlefehldt et al., 1996](#); [McCoy et al., 1997a,b](#); [Floss, 2000](#); [Dhaliwal et al., 2017](#); [Keil and McCoy, 2018](#); [Lucas et al., 2022](#)). The degrees of melting (F) of OC at 1200 °C range between ~15–25% ([Collinet and Grove, 2020b](#)), and there is a decent match between Néma 001's olivine-free major element composition and that of OC partial melts at the lower end of that range around F of ~15% (Supp. Figure 4). A range of 15–20% melting is also consistent with incompatible REE abundances being enriched by 5–6 times in Néma 001 compared to an H chondrite composition for example (e.g., a ~F enrichment factor; [Barrat et al., 2021](#)). The bulk Sr, Ti, and REE abundances of Néma 001 are also in line with those of silicate melts produced by 10–15% disequilibrium partial melting of an OC starting composition over a week (Figure 7b), suggesting that Néma 001 melts were rapidly extracted from their source regions, as suggested for the evolved clast ALM-A from the Almahata Sitta polymict meteorite ([Bischoff et al., 2014](#)). At these conditions, MELTS calculations suggest that partial melting also produced ~25% Fe-Ni melts (Table S12, [Tartèse et al., 2025](#)).

We proposed earlier that olivine in Néma 001 could be a restite phase inherited from partial melting residues, having notably a typical size of ca. 500–750 µm similar to that of olivine in lodranites that have experienced 5 to > 10% partial melting ([McCoy et al., 1997b](#)). However, olivine in Néma 001 (Fo<sub>77</sub>) is less magnesian than in lodranites

(typically between Fo<sub>90</sub>–Fo<sub>85</sub>; e.g., [Keil and McCoy, 2018](#)). Exchange of Fe and Mg between olivine and melt is rapid; modelling by [Mourey et al. \(2023\)](#) suggests that it would only take a couple of decades to completely homogenise a 1 mm-long olivine from an original Fo<sub>90</sub> to a final Fo<sub>80</sub> composition at ~1200 °C (olivine elongated along the c-axis where diffusion is the slowest). The melt composition would then progressively evolve as crystallisation proceeded. Using the Mg# of orthopyroxene (80) and clinopyroxene (86) in Néma 001 and  $K_D^{Mg-Fe}$  exchange coefficients of  $0.28 \pm 0.05$  and  $0.25 \pm 0.05$  (e.g., [Beattie, 1993](#); [Neave et al., 2024](#); [Toplis, 2005](#)), respectively, yields melts Mg# in the range ~53–60 ± 5. Therefore, the first melts that interacted with restite olivine (with an original composition of Fo<sub>90</sub>–Fo<sub>85</sub>, similar to lodranite olivine) may have had Mg# values around 75. With progressive crystallisation of pyroxene, the melt Mg# decreased, as recorded by orthopyroxene and clinopyroxene compositions (Figure 3a). The lack of zoning in any of the major minerals suggest slow cooling, with a final subsolidus pyroxene equilibration temperature of ca. 900 °C.

#### 4.2 Comparing Néma 001 to other achondrite meteorites

The bulk oxygen isotope composition of Néma 001, both in terms of  $\delta^{18}O$  and  $\Delta^{17}O$  values, is similar to that of most acapulcoites and lodranites (Figure 5a). This is consistent with derivation of Néma 001 from the acapulcoite-lodranite asteroidal parent body. This is also supported by the olivine and pyroxene Fe/Mn ratios that are similar for Néma 001 and Lodran (Supp. Figure 5), as well as by similar chromite compositions (Figure 3d). In contrast, Néma 001 bulk oxygen isotope composition differs from that of most of the other main achondrite groups and ungrouped achondrites, except for the ungrouped achondrites Northwest Africa (NWA) 6693/6704/10132 (which are likely paired; [Greenwood et al., 2017](#)) that have similar oxygen isotope compositions to Néma 001 (Figure 5a). However, the pyroxene Fe/Mn molar ratios (~67 to 95; [Warren et al., 2013](#); [Hibiya et al., 2019](#)) of these meteorites are much higher than in pyroxenes in Néma 001, indicating that Néma 001 and NWA 6693/6704/10132 originated from a distinct parent body. As mentioned in Section 3.2.1,  $\epsilon^{54}Cr$  and  $\epsilon^{50}Ti$  isotope anomalies also show that these latter meteorites are carbonaceous achondrites that cannot be genetically related to the non-carbonaceous acapulcoites-lodranites (e.g., [Sanborn et al., 2019](#)).

As stated in the Results section, pyroxenes in Néma 001 are more magnesian than in other ungrouped achondrites, but less magnesian than in acapulcoites, lodranites, gabbroic clasts in LEW 86220, and FRO 93001 (Figure 3a). Similar Fe/Mn, but higher Fe/Mg ratios is what one would expect for pyroxenes crystallising from a melt complementary to lodranite-like residues, similarly to the observed relationship between mafic mineral compositions in GRA 06128/06129 and brachinites (e.g., [Day et al., 2012](#)).



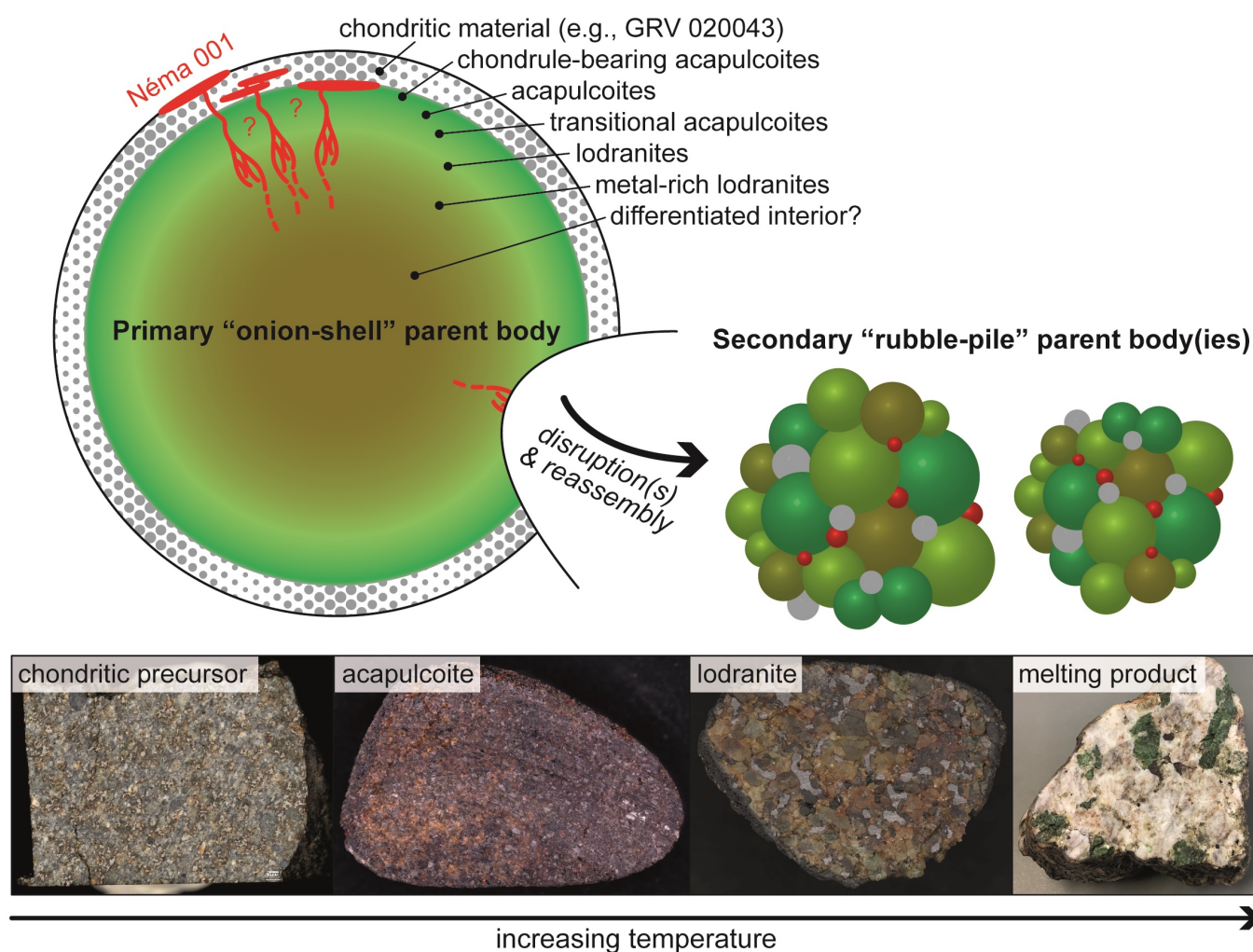


**Figure 13.** Schematic depiction and evolution of the GRV 020043-acapulcoite-lodranite-Néma 001 parent body (adapted from Lucas et al., 2022). The samples of chondrite, acapulcoite (Akka 001), lodranite (NWA 6562), and Néma 001 are from the CERGE collection.

### 4.3 Searching for Néma 001's parent asteroid

To investigate possible asteroidal parent bodies, we obtained reflectance spectra on a powdered sample and a polished thick section of Néma 001. On the thick section, point spectra were measured on different areas of the sample, and regions were identified with spectra typical of olivine and areas assigned as being clinopyroxene-rich (Figure 11a). We did not identify areas dominated by orthopyroxene signature at our spatial resolution (6 mm diameter). Spectra obtained on the clinopyroxene-rich areas show a clear absorption around 0.7  $\mu\text{m}$  that may be attributed to the presence of chromium (Cloutis, 2002). In order to assess the reflectance spectrum of the bulk sample based on these point measurements, we did a simple linear mixing model of spectra obtained on olivine- and clinopyroxene-rich areas (Figure 11b). This calculation neglects the effect of plagioclase, that is spectrally neutral and whose presence would lead to an overall decrease of the strength of absorption bands. Results of this calculation show a very good agreement with measurements obtained on the powdered sample (Figure 11b). The reflectance spectrum of Néma 001 powder is quite distinct compared to

spectra of meteorites from the Howardite-Eucrite-Diogenite group, as well as from spectra of Acapulcoite-Lodranites (Figure 11). The 1- $\mu\text{m}$  band for an asteroid related to Néma 001 would likely be unusually broad, given the contribution from clinopyroxene and olivine, when compared to abundant basaltic objects such as vestoids. Also, the relative ratio of the 2- $\mu\text{m}$  and 1- $\mu\text{m}$  bands will be low, unlike what is observed for diogenites (including olivine-rich diogenite). These properties would make the parent body of Néma 001 identifiable based on reflectance spectroscopy, if the surface is intact and Néma 001-like material is exposed there. The green colour of Cr-rich clinopyroxene of a Néma 001-covered asteroid could be identifiable based on multi-colour survey, but the effects of space-weathering are particularly strong in the visible range and may quickly change the visible colours.

There exist asteroid taxonomic types with signatures similar, though not identical, to those obtained for Néma 001. They are the O-type and Q-type (DeMeo et al., 2009; Mahlke et al., 2022). These visual matches were further assessed using the taxonomic classification tool of Mahlke et al. (2022). This revealed that, although no perfect match was found, the O-type are the closest

taxonomic classes (Figure 12). While comparison to our model suggests possible connections between Néma 001 and these asteroidal end-members, finer examination shows that the 1- $\mu\text{m}$  band position is slightly different between the Néma 001 model and Q-type, and that the relative band depth between the 1- and 2- $\mu\text{m}$  band are different between O-type and Néma 001 model. Also, the absorption around 0.7  $\mu\text{m}$  observed for Néma 001 is not observed in any of the taxonomic endmembers, but this band may be particularly sensitive to space-weathering processes. Investigations of the effect of space-weathering on this meteorite of fairly unusual mineralogy may help find possible source asteroids.

#### 4.4 Implications for the acapulcoite-lodranite-Néma 001 asteroidal parent body

It has been proposed that the acapulcoites and lodranites originated from a complex layered parent body, with size estimates ranging from  $\sim 25$ – $100$  km radius (Touboul et al., 2009; Golabek et al., 2014; Li et al., 2018; Lucas et al., 2022) and up to  $260$  km radius (Neumann et al., 2018). This parent body, from the outside surface inwards, may have originally comprised of an undifferentiated chondritic outer shell akin the Grove Mountains (GRV) 020043 type 4 chondrite, an acapulcoite-like layer, an acapulcoite-lodranite transitional horizon, and a lodranite-like layer with increasing amounts of Fe-Ni metal with increasing depth (Li et al., 2018; Lucas et al., 2022, Figure 13). Neumann et al. (2018) even suggested that the body was fully differentiated, containing a metallic core and a silicate mantle underneath the acapulcoite-lodranite horizons. At  $1200$   $^{\circ}\text{C}$ , a melt with the bulk composition of Néma 001 would have a density of  $2500$ – $2600$   $\text{kg}\cdot\text{m}^{-3}$  (Supp. Figure 6). The model of Neumann et al. (2018) suggests that the acapulcoite-lodranite parent body would have been comprised of a  $\sim 1$  km chondritic porous outer shell with a density of  $\sim 2700$   $\text{kg}\cdot\text{m}^{-3}$  (for an initial porosity set at 30 vol%), a chondritic compacted layer with a density of  $\sim 3900$   $\text{kg}\cdot\text{m}^{-3}$  down to a depth of  $\sim 10$  km, followed by a  $\sim 4$  km thick partially differentiated layer where the density decreases to  $\sim 3300$   $\text{kg}\cdot\text{m}^{-3}$ . If silicate melts produced by partial melting of lodranite precursors had densities similar to that calculated for Néma 001, it is likely that these melts would have ascended from their source region because of the density contrast with surrounding host rocks (Figure 13). Whether these melts would have been able to migrate upwards through the outermost porous chondritic shell depends on many factors, such as initial porosity – with a slight increase of porosity to 35 vol% from the value of 30 vol% used in the Neumann et al. (2018) model, the density for the porous outer shell decreases to  $\sim 2500$   $\text{kg}\cdot\text{m}^{-3}$ , slightly lower than the predicted Néma 001 parent melt density. Finally, we note that the coarse grain size of Néma 001 suggests that it crystallised slowly either in a plutonic intrusion at depth or in the interior of a thick lava flow if melts reached the surface.

Most modelling studies suggest that acapulcoite-lodranite meteorites originated from  $\sim 7$ – $25$  km depth from a  $\sim 25$ – $260$  km radius parent body that accreted  $1.5 \pm 0.2$  Ma

after the formation of CAIs and that peak temperatures of  $\sim 1200$ – $1300$   $^{\circ}\text{C}$  for lodranites occurred ca.  $2.5$ – $4$  Ma after CAIs (e.g., Touboul et al., 2009; Golabek et al., 2014; Neumann et al., 2018). Bulk MC-ICP-MS and in situ SIMS Al/Mg analyses yielded distinct dates of  $3.3 \pm 0.2$  Ma and  $6.6 \pm 0.6$  Ma after the formation of CAIs (Figure 8), which correspond to the closure of ferromagnesian phases (olivine, pyroxene) and plagioclase to Mg diffusion, respectively. For instance, calculation of this closure temperature for albite, enstatite, and forsterite, all taken as cylinders with radii of  $0.5$ – $1$  mm, akin to those observed in Néma 001 (Figure 2), yields temperatures of  $\sim 750$ – $900$   $^{\circ}\text{C}$  for albite,  $\sim 1030$ – $1400$   $^{\circ}\text{C}$  for forsterite, and  $\sim 1120$ – $1550$   $^{\circ}\text{C}$  for enstatite for cooling rates of  $0.1$ – $10$   $^{\circ}\text{C}/\text{yr}$  (Supp. Figure 7), which are those obtained by Lucas et al. (2022) for the first phase of fast cooling for acapulcoites-lodranites. In thermal evolution models that postulate monotonic cooling for the acapulcoite-lodranite parent body, peak temperatures of  $\sim 1200$ – $1300$   $^{\circ}\text{C}$  are reached at  $\sim 3$ – $4$  Ma after CAIs in the lodranite source regions, which then cool down to temperatures of  $700$ – $900$   $^{\circ}\text{C}$  around  $7$  Ma after CAIs (Touboul et al., 2009; Neumann et al., 2018). The discordant Al/Mg dates of  $3.3 \pm 0.2$  Ma and  $6.6 \pm 0.6$  Ma after CAIs recorded by ferromagnesian silicates and plagioclase are thus fully consistent with these thermal evolution models, and with formation of Néma 001 melts by partial melting of lodranite precursors during peak metamorphism in the acapulcoite-lodranite parent body. However, by compiling a wide range of cooling rate estimates, Lucas et al. (2022) argued that the acapulcoite-lodranite parent body underwent a first stage of fast cooling at  $\sim 0.1$ – $10$   $^{\circ}\text{C}/\text{yr}$  from peak temperature to  $\sim 750$   $^{\circ}\text{C}$ , followed by slower cooling at  $\sim 0.001$ – $0.1$   $^{\circ}\text{C}/\text{yr}$  below  $\sim 750$   $^{\circ}\text{C}$ , which is not consistent with undisturbed monotonous cooling in a layered asteroid. Instead, they proposed that the original parent body was disrupted by an impact event shortly after its formation, producing fragments with radii of  $\sim 0.3$ – $10$  km that re-accreted within a few thousand years into one or several rubble-pile asteroids (Figure 13). In the Acapulco meteorite, apatite Pb/Pb dating yielded a date of  $4556.5 \pm 1.3$  Ma (Amelin, 2005), which may correspond to this early break-up event (Lucas et al., 2022). This is also consistent with an I-Xe age of  $\sim 4558$  Ma obtained on Acapulco and the lodranite GRA 95209 (Crowther et al., 2009). In such scenario the Al/Mg date of  $6.6 \pm 0.6$  Ma after CAIs recorded by plagioclase in Néma 001 may correspond to a complete resetting of the Al/Mg chronometer at temperatures exceeding the plagioclase closure temperature to Mg diffusion during early break-up and reassembly of the acapulcoite-lodranite parent body. Plagioclase  $^{40}\text{Ar}/^{39}\text{Ar}$  and apatite U-Pb dating in Néma 001 yielded identical, younger dates of  $4.48$  Ga, which are at the lower end of the range of Ar/Ar dates of  $4.49$ – $4.52$  Ga obtained on acapulcoite-lodranite meteorites (Bogard, 2011). To a first order, the Ar/Ar and apatite U-Pb closure temperatures of  $\sim 500 \pm 100$   $^{\circ}\text{C}$  are similar (Pellas et al., 1997; Cochran et al., 2014; Schoene and Bowring, 2007). Cooling from  $750$  to  $500$   $^{\circ}\text{C}$  between  $4555$  and  $4520$ – $4480$  Ma yields cooling

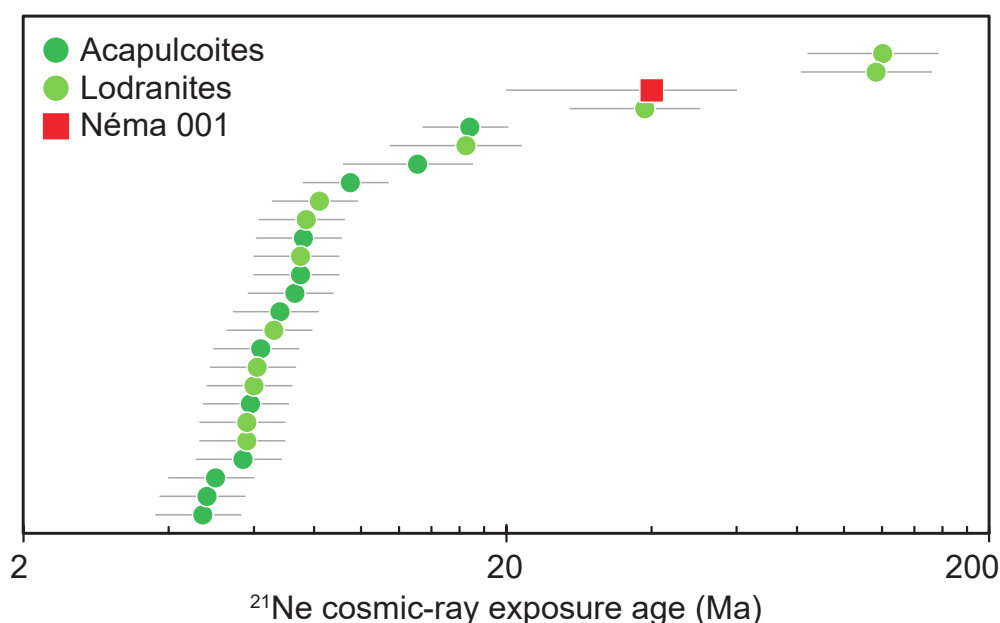


**Figure 14.** Comparison of the  $^{21}\text{Ne}$  cosmic-ray exposure age of Néma 001 with  $^{21}\text{Ne}$  cosmic-ray exposure ages determined for acapulcoites and lodranites (Weigel et al., 1999; Patzer et al., 2003; Eugster and Lorenzetti, 2005; Smith et al., 2023).

rates of  $\sim 3\text{--}7 \times 10^{-6} \text{ }^\circ\text{C/yr}$ , orders of magnitude slower than estimates for acapulcoites-lodranites (Lucas et al., 2022). Therefore, we interpret the Néma 001 plagioclase  $^{40}\text{Ar}/^{39}\text{Ar}$  and apatite U-Pb dates of 4.48 Ga as dating the timing of a later impact event. Finally, our best estimate for the  $^{21}\text{Ne}$  CRE age of Néma 001 of  $40 \pm 20 \text{ Ma}$  is consistent with that of the lodranite NWA 7474 (Figure 14). These CRE age data implies that meteorites from the parent asteroid(s) of the acapulcoites and lodranites were delivered to the Earth following multiple break-up events at ca. 5–10 Ma,  $\sim 15 \text{ Ma}$ ,  $\sim 40 \text{ Ma}$ , and  $\sim 100\text{--}150 \text{ Ma}$  (Figure 14).

## 5 Conclusions

The mineralogy, chemistry, and chronological history of Néma 001 are all consistent with an origin from a partially differentiated asteroidal parent body, for which the acapulcoite-lodranite meteorites represent partial melting residues. Similarly to the other ungrouped achondrites GRA 06128/06129, ALM-A, and Erg Chech 002, Néma 001 has an andesitic composition that is consistent with compositions of silicate melts produced by partial melting of ordinary chondrite-like precursors during the first few millions of years of evolution of the Solar System. With the addition of Néma 001, we now have a comprehensive suite of samples from the acapulcoite-lodranite parent body, including unmelted chondritic precursor material, residues from  $\sim 1\text{--}20\%$  partial melting, and variably differentiated igneous rocks. This unique suite of samples is key to further investigate melting and differentiation processes of asteroids, and supports the existence of partially differentiated planetesimals.

## Acknowledgments

RT acknowledges funding from the UK Science and Technology Facilities Council (STFC) (#ST/P005225/1), the University of Manchester and STFC (grant #ST/S002170/1) for funding the LA-ICP-MS facility in Manchester, and the Royal Society for funding the benchtop SEM in Manchester. KHJ acknowledges funding by the Royal Society (URF\R\201009, URF\ERE\210158) and STFC (ST/V000675/1 and ST/Y002318/1). This project has received funding the European Research Council (ERC) under the European Union's Horizon Europe research and innovation program (grant agreement no. 101041122 to G. Avice). VD thanks the FRS-FNRS and EoS project "ET-HoME" for support. GH thanks the FNRS PDR "COOL" for funding. VD and GH thank Dina Cabrita, Jeroen De Jong, Wendy Debouge and Sixtine Paitoni at ULB for help with measurements. JV thanks l'Agence Nationale de la Recherche (grant CASSYSS ANR-18-CE31-0010-01 - PI Johan Villeneuve) for funding LG-SIMS analyses. We thank Ray Burgess for his help with the argon data collection and interpretation, and the journal editors and reviewers for their helpful suggestions.

## Data, code, and outputs availability

Supporting figures and data used in the manuscript are available in the accompanying Supplementary Material and the data publication of Tartèse et al. (2025, <https://doi.org/10.48420/29126567.v3>), respectively. Main text figures are available for download in the online version of this article.



## Licence agreement

This article is distributed under the terms of the Creative Commons Attribution 4.0 International Licence (CC BY 4.0), which permits unrestricted use, distribution, and reproduction in any medium, provided appropriate credit is given to the original author(s) and source, as well as a link to the Creative Commons licence, and an indication of changes that were made.

## References

- Alexandre A, Basile-Doelsch I, Sonzogni C, Sylvestre F, Parron C, Meunier JD, Colin F (2006). Oxygen isotope analyses of fine silica grains using laser-extraction technique: Comparison with oxygen isotope data obtained from ion microprobe analyses and application to quartzite and silcrete cement investigation. *Geochimica et Cosmochimica Acta* 70(11): 2827–2835. doi:10.1016/j.gca.2006.03.003.
- Amelin Y (2005). Meteorite phosphates show constant  $^{176}\text{Lu}$  decay rate since 4557 million years ago. *Science* 310(5749): 839–841. doi:10.1126/science.1117919.
- Apen FE, Wall CJ, Cottle JM, Schmitz MD, Kylander-Clark AR, Seward GG (2022). Apatites for destruction: Reference apatites from Morocco and Brazil for U-Pb petrochronology and Nd and Sr isotope geochemistry. *Chemical Geology* 590: 120689. doi:10.1016/j.chemgeo.2021.120689.
- Avice G, Kendrick M, Richard A, Ferrière L (2023). Ancient atmospheric noble gases preserved in post-impact hydrothermal minerals of the 200 Ma-old Rochechouart impact structure, France. *Earth and Planetary Science Letters* 620: 118351. doi:10.1016/j.epsl.2023.118351.
- Barrat J, Greenwood R, Verchovsky A, Gillet P, Bollinger C, Langlade J, Liorzou C, Franchi I (2015). Crustal differentiation in the early solar system: Clues from the unique achondrite Northwest Africa 7325 (NWA 7325). *Geochimica et Cosmochimica Acta* 168: 280–292. doi:10.1016/j.gca.2015.07.020.
- Barrat J, Zanda B, Moynier F, Bollinger C, Liorzou C, Bayon G (2012). Geochemistry of CI chondrites: Major and trace elements, and Cu and Zn Isotopes. *Geochimica et Cosmochimica Acta* 83: 79–92. doi:10.1016/j.gca.2011.12.011.
- Barrat JA, Chaussidon M, Yamaguchi A, Beck P, Villeneuve J, Byrne DJ, Broadley MW, Marty B (2021). A 4,565-My-old andesite from an extinct chondritic protoplanet. *Proceedings of the National Academy of Sciences* 118(11). doi:10.1073/pnas.2026129118.
- Basunia M, Hurst A (2016). Nuclear Data Sheets for A = 26. *Nuclear Data Sheets* 134: 1–148. doi:10.1016/j.nds.2016.04.001.
- Beattie P (1993). Olivine-melt and orthopyroxene-melt equilibria. *Contributions to Mineralogy and Petrology* 115(1): 103–111. doi:10.1007/bf00712982.
- Bischoff A, Horstmann M, Barrat JA, Chaussidon M, Pack A, Herwartz D, Ward D, Vollmer C, Decker S (2014). Trachyandesitic volcanism in the early Solar System. *Proceedings of the National Academy of Sciences* 111(35): 12689–12692. doi:10.1073/pnas.1404799111.
- Bogard DD (2011). K–Ar ages of meteorites: Clues to parent-body thermal histories. *Geochemistry* 71(3): 207–226. doi:10.1016/j.chemer.2011.03.001.
- Brey GP, Köhler T (1990). Geothermobarometry in Four-phase Lherzolites II. New Thermobarometers, and Practical Assessment of Existing Thermobarometers. *Journal of Petrology* 31(6): 1353–1378. doi:10.1093/petrology/31.6.1353.
- Bryson JFJ, Weiss BP, Getzin B, Abrahams JNH, Nimmo F, Scholl A (2019). Paleomagnetic Evidence for a Partially Differentiated Ordinary Chondrite Parent Asteroid. *Journal of Geophysical Research: Planets* 124(7): 1880–1898. doi:10.1029/2019je005951.
- Bussweiler Y, Giuliani A, Greig A, Kjarsgaard B, Petts D, Jackson S, Barrett N, Luo Y, Pearson D (2019). Trace element analysis of high-Mg olivine by LA-ICP-MS – Characterization of natural olivine standards for matrix-matched calibration and application to mantle peridotites. *Chemical Geology* 524: 136–157. doi:10.1016/j.chemgeo.2019.06.019.
- Carporzen L, Weiss BP, Elkins-Tanton LT, Shuster DL, Ebel D, Gattacceca J (2011). Magnetic evidence for a partially differentiated carbonaceous chondrite parent body. *Proceedings of the National Academy of Sciences* 108(16): 6386–6389. doi:10.1073/pnas.1017165108.
- Cattani F, Avice G, Ferrière L, Alwmark S (2024). Noble gases in shocked igneous rocks from the 380 Ma-old Siljan impact structure (Sweden): A search for paleo-atmospheric signatures. *Chemical Geology* 670: 122440. doi:10.1016/j.chemgeo.2024.122440.
- Chew D, Petrus J, Kamber B (2014). U–Pb LA–ICPMS dating using accessory mineral standards with variable common Pb. *Chemical Geology* 363: 185–199. doi:10.1016/j.chemgeo.2013.11.006.
- Chew DM, Babechuk MG, Cogné N, Mark C, O'Sullivan GJ, Henrichs IA, Doepe D, McKenna CA (2016). (LA,Q)-ICPMS trace-element analyses of Durango and McClure Mountain apatite and implications for making natural LA-ICPMS mineral standards. *Chemical Geology* 435: 35–48. doi:10.1016/j.chemgeo.2016.03.028.
- Clayton RN (1993). Oxygen Isotopes in Meteorites. *Annual Review of Earth and Planetary Sciences* 21(1): 115–149. doi:10.1146/annurev.earth.21.050193.000555.
- Cloutis EA (2002). Pyroxene reflectance spectra: Minor absorption bands and effects of elemental substitutions. *Journal of Geophysical Research: Planets* 107(E6). doi:10.1029/2001je001590.
- Cochrane R, Spikings RA, Chew D, Wotzlaw JF, Chiaradia M, Tyrrell S, Schaltegger U, Van der Lelij R (2014). High temperature (>350°C) thermochronology and mechanisms of Pb loss in apatite. *Geochimica et Cosmochimica Acta* 127: 39–56. doi:10.1016/j.gca.2013.11.028.
- Collinet M, Grove TL (2020a). Formation of primitive achondrites by partial melting of alkali-undepleted planetesimals in the inner solar system. *Geochimica et Cosmochimica Acta* 277: 358–376. doi:10.1016/j.gca.2020.03.004.
- Collinet M, Grove TL (2020b). Widespread production of silica- and alkali-rich melts at the onset of planetesimal melting. *Geochimica et Cosmochimica Acta* 277: 334–357. doi:10.1016/j.gca.2020.03.005.
- Cournède C, Gattacceca J, Rochette P, Shuster D (2020). Paleomagnetism of Rumuruti chondrites suggests a partially differentiated parent body. *Earth and Planetary Science Letters* 533: 116042. doi:10.1016/j.epsl.2019.116042.
- Crowther SA, Whitby JA, Busfield A, Holland G, Busemann H, Gilmour JD (2009). Collisional modification of the acapulcoite/lodranite parent body revealed by the iodine-xenon system in lodranites. *Meteoritics & Planetary Science* 44(8): 1151–1159. doi:10.1111/j.1945-5100.2009.tb01214.x.
- Dauphas N, Chaussidon M (2011). A Perspective from Extinct Radionuclides on a Young Stellar Object: The Sun and Its Accretion Disk. *Annual Review of Earth and Planetary Sciences* 39(1): 351–386. doi:10.1146/annurev-earth-040610-133428.
- Day JM, Walker RJ, Ash RD, Liu Y, Rumble D, Irving AJ, Goodrich CA, Tait K, McDonough WF, Taylor LA (2012). Origin of felsic achondrites Graves Nunataks 06128 and 06129, and ultramafic brachinites and brachinite-like achondrites by partial melting of volatile-rich primitive parent bodies. *Geochimica et Cosmochimica Acta* 81: 94–128. doi:10.1016/j.gca.2011.12.017.

- Day JMD, Ash RD, Liu Y, Bellucci JJ, III DR, McDonough WF, Walker RJ, Taylor LA (2009). Early formation of evolved asteroidal crust. *Nature* 457(7226): 179–182. doi:10.1038/nature07651.
- DeMeo FE, Binzel RP, Slivan SM, Bus SJ (2009). An extension of the Bus asteroid taxonomy into the near-infrared. *Icarus* 202(1): 160–180. doi:10.1016/j.icarus.2009.02.005.
- Dhaliwal JK, Day JM, Corder CA, Tait KT, Marti K, Assayag N, Cartigny P, Rumble D, Taylor LA (2017). Early metal-silicate differentiation during planetesimal formation revealed by acapulcoite and lodranite meteorites. *Geochimica et Cosmochimica Acta* 216: 115–140. doi:10.1016/j.gca.2017.06.042.
- Easton A (1985). SEVEN NEW BULK CHEMICAL ANALYSES OF AUBRITES. *Meteoritics* 20(3): 571–573. doi:10.1111/j.1945-5100.1985.tb00052.x.
- Elkins-Tanton LT, Weiss BP, Zuber MT (2011). Chondrites as samples of differentiated planetesimals. *Earth and Planetary Science Letters* 305(1–2): 1–10. doi:10.1016/j.epsl.2011.03.010.
- Eugster O, Lorenzetti S (2005). Cosmic-ray exposure ages of four acapulcoites and two differentiated achondrites and evidence for a two-layer structure of the acapulcoite/lodranite parent asteroid. *Geochimica et Cosmochimica Acta* 69(10): 2675–2685. doi:10.1016/j.gca.2004.12.006.
- Eugster O, Michel T (1995). Common asteroid break-up events of eucrites, diogenites, and howardites and cosmic-ray production rates for noble gases in achondrites. *Geochimica et Cosmochimica Acta* 59(1): 177–199. doi:10.1016/0016-7037(94)00327-i.
- Feldstein SN, Jones RH, Papike JJ (2001). Disequilibrium partial melting experiments on the Leedey L6 chondrite: Textural controls on melting processes. *Meteoritics & Planetary Science* 36(11): 1421–1441. doi:10.1111/j.1945-5100.2001.tb01836.x.
- Floss C (2000). Complexities on the acapulcoite-lodranite parent body: Evidence from trace element distributions in silicate minerals. *Meteoritics & Planetary Science* 35(5): 1073–1085. doi:10.1111/j.1945-5100.2000.tb01494.x.
- Folco L, D’Orazio M, Burrone A (2006). Frontier Mountain 93001: A coarse-grained, enstatite-augite-oligoclase-rich, igneous rock from the acapulcoite-lodranite parent asteroid. *Meteoritics & Planetary Science* 41(8): 1183–1198. doi:10.1111/j.1945-5100.2006.tb00515.x.
- Galy A, Yoffe O, Janney PE, Williams RW, Cloquet C, Alard O, Halicz L, Wadhwa M, Hutcheon ID, Ramon E, Carignan J (2003). Magnesium isotope heterogeneity of the isotopic standard SRM980 and new reference materials for magnesium-isotope-ratio measurements. *Journal of Analytical Atomic Spectrometry* 18(11): 1352. doi:10.1039/b309273a.
- Gattacceca J, Weiss BP, Gounelle M (2016). New constraints on the magnetic history of the CV parent body and the solar nebula from the Kaba meteorite. *Earth and Planetary Science Letters* 455: 166–175. doi:10.1016/j.epsl.2016.09.008.
- Golabek GJ, Bourdon B, Gerya TV (2014). Numerical models of the thermomechanical evolution of planetesimals: Application to the acapulcoite-lodranite parent body. *Meteoritics & Planetary Science* 49(6): 1083–1099. doi:10.1111/maps.12302.
- Greenwood R, Franchi I, Gibson J, Benedix G (2012). Oxygen isotope variation in primitive achondrites: The influence of primordial, asteroidal and terrestrial processes. *Geochimica et Cosmochimica Acta* 94: 146–163. doi:10.1016/j.gca.2012.06.025.
- Greenwood RC, Burbine TH, Miller MF, Franchi IA (2017). Melting and differentiation of early-formed asteroids: The perspective from high precision oxygen isotope studies. *Geochemistry* 77(1): 1–43. doi:10.1016/j.chemer.2016.09.005.
- Gualda GAR, Ghiorso MS, Lemons RV, Carley TL (2012). Rhyolite-MELTS: a Modified Calibration of MELTS Optimized for Silica-rich, Fluid-bearing Magmatic Systems. *Journal of Petrology* 53(5): 875–890. doi:10.1093/petrology/egr080.
- Hennessy J, Turner G (1980). 40Ar–39Ar ages and irradiation history of Luna 24 basalts. *Philosophical Transactions of the Royal Society of London Series A, Mathematical and Physical Sciences* 297(1428): 27–39. doi:10.1098/rsta.1980.0202.
- Hevey PJ, Sanders IS (2006). A model for planetesimal meltdown by 26Al and its implications for meteorite parent bodies. *Meteoritics & Planetary Science* 41(1): 95–106. doi:10.1111/j.1945-5100.2006.tb00195.x.
- Hibiya Y, Archer GJ, Tanaka R, Sanborn ME, Sato Y, Iizuka T, Ozawa K, Walker RJ, Yamaguchi A, Yin QZ, Nakamura T, Irving AJ (2019). The origin of the unique achondrite Northwest Africa 6704: Constraints from petrology, chemistry and Re–Os, O and Ti isotope systematics. *Geochimica et Cosmochimica Acta* 245: 597–627. doi:10.1016/j.gca.2018.04.031.
- Howell D, Griffin W, Pearson N, Powell W, Wieland P, O’Reilly S (2013). Trace element partitioning in mixed-habit diamonds. *Chemical Geology* 355: 134–143. doi:10.1016/j.chemgeo.2013.07.013.
- Hublet G, Debaille V, Wimpenny J, Yin QZ (2017). Differentiation and magmatic activity in Vesta evidenced by 26Al–26Mg dating in eucrites and diogenites. *Geochimica et Cosmochimica Acta* 218: 73–97. doi:10.1016/j.gca.2017.09.005.
- Hunt AC, Benedix GK, Hammond SJ, Bland PA, Rehkämper M, Kreissig K, Strekopytov S (2017). A geochemical study of the winonaites: Evidence for limited partial melting and constraints on the precursor composition. *Geochimica et Cosmochimica Acta* 199: 13–30. doi:10.1016/j.gca.2016.10.043.
- Härtel B, Matthews WA, Enkelmann E (2023). Duluth Complex FC1 Apatite and Zircon: Reference Materials for (U–Th)/He Dating? *Geostandards and Geoanalytical Research* 47(3): 669–681. doi:10.1111/ggr.12492.
- Jacobsen B, Yin Qz, Moynier F, Amelin Y, Krot AN, Nagashima K, Hutcheon ID, Palme H (2008). 26Al–26Mg and 207Pb–206Pb systematics of Allende CAIs: Canonical solar initial 26Al/27Al ratio reinstated. *Earth and Planetary Science Letters* 272(1–2): 353–364. doi:10.1016/j.epsl.2008.05.003.
- Jochum KP, Willbold M, Raczek I, Stoll B, Herwig K (2005). Chemical Characterisation of the USGS Reference Glasses GSA-1G, GSC-1G, GSD-1G, GSE-1G, BCR-2G, BHVO-2G and BIR-1G Using EPMA, ID-TIMS, ID-ICP-MS and LA-ICP-MS. *Geostandards and Geoanalytical Research* 29(3): 285–302. doi:10.1111/j.1751-908x.2005.tb00901.x.
- Jurewicz A, Mittlefehldt D, Jones J (1995). Experimental partial melting of the St. Severin (LL) and Lost City (H) chondrites. *Geochimica et Cosmochimica Acta* 59(2): 391–408. doi:10.1016/0016-7037(94)00328-j.
- Keil K (2012). Angrites, a small but diverse suite of ancient, silica-undersaturated volcanic-plutonic mafic meteorites, and the history of their parent asteroid. *Geochemistry* 72(3): 191–218. doi:10.1016/j.chemer.2012.06.002.
- Keil K, McCoy TJ (2018). Acapulcoite-lodranite meteorites: Ultramafic asteroidal partial melt residues. *Geochemistry* 78(2): 153–203. doi:10.1016/j.chemer.2017.04.004.
- Kleine T, Mezger K, Palme H, Scherer E, Münker C (2005). Early core formation in asteroids and late accretion of chondrite parent bodies: Evidence from 182Hf–182W in CAIs, metal-rich chondrites, and iron meteorites. *Geochimica et Cosmochimica Acta* 69(24): 5805–5818. doi:10.1016/j.gca.2005.07.012.

- Kleine T, Touboul M, Bourdon B, Nimmo F, Mezger K, Palme H, Jacobsen SB, Yin QZ, Halliday AN (2009). Hf–W chronology of the accretion and early evolution of asteroids and terrestrial planets. *Geochimica et Cosmochimica Acta* 73(17): 5150–5188. doi:10.1016/j.gca.2008.11.047.
- Krot A, Keil K, Scott E, Goodrich C, Weisberg M (2014). *Classification of Meteorites and Their Genetic Relationships*, p. 1–63. Elsevier. doi:10.1016/b978-0-08-095975-7.00102-9.
- Li S, Yin QZ, Bao H, Sanborn ME, Irving A, Ziegler K, Agee C, Marti K, Miao B, Li X, Li Y, Wang S (2018). Evidence for a multilayered internal structure of the chondritic acapulcoite-lodranite parent asteroid. *Geochimica et Cosmochimica Acta* 242: 82–101. doi:10.1016/j.gca.2018.09.004.
- Liang Y, Sun C, Yao L (2013). A REE-in-two-pyroxene thermometer for mafic and ultramafic rocks. *Geochimica et Cosmochimica Acta* 102: 246–260. doi:10.1016/j.gca.2012.10.035.
- Lindsay FN, Herzog GF, Park J, Delaney JS, Turrin BD, Swisher CC (2014). <sup>40</sup>Ar/<sup>39</sup>Ar dating of microgram feldspar grains from the paired feldspathic achondrites GRA 06128 and 06129. *Geochimica et Cosmochimica Acta* 129: 96–110. doi:10.1016/j.gca.2013.12.023.
- Lucas MP, Dygert N, Ren J, Hesse MA, Miller NR, McSween HY (2022). Thermochemical evolution of the acapulcoite-lodranite parent body: Evidence for fragmentation-disrupted partial differentiation. *Meteoritics & Planetary Science* 57(12): 2248–2275. doi:10.1111/maps.13930.
- Mahlke M, Carry B, Mattei PA (2022). Asteroid taxonomy from cluster analysis of spectrometry and albedo. *Astronomy & Astrophysics* 665: A26. doi:10.1051/0004-6361/202243587.
- Mason B (1967). Meteorites. *Am Sci* 55: 429–455.
- McCoy T, Keil K, Clayton R, Mayeda T, Bogard D, Garrison D, Wieler R (1997a). A petrologic and isotopic study of lodranites: Evidence for early formation as partial melt residues from heterogeneous precursors. *Geochimica et Cosmochimica Acta* 61(3): 623–637. doi:10.1016/s0016-7037(96)00359-6.
- McCoy T, Keil K, Muenow D, Wilson L (1997b). Partial melting and melt migration in the acapulcoite-lodranite parent body. *Geochimica et Cosmochimica Acta* 61(3): 639–650. doi:10.1016/s0016-7037(96)00365-1.
- McCoy T J, Corrigan CM, Dickinson TL, Benedix GK, Schrader DL, Davidson J (2019). Grove Mountains (GRV) 020043: Insights into acapulcoite-lodranite genesis from the most primitive member. *Geochimistry* 79(4): 125536. doi:10.1016/j.chemer.2019.125536.
- Mittlefehldt DW (2015). Asteroid (4) Vesta: I. The howardite-eucrite-diogenite (HED) clan of meteorites. *Geochimistry* 75(2): 155–183. doi:10.1016/j.chemer.2014.08.002.
- Mittlefehldt DW, Lindstrom MM, Bogard DD, Garrison DH, Field SW (1996). Acapulco- and Lodran-like achondrites: Petrology, geochemistry, chronology, and origin. *Geochimica et Cosmochimica Acta* 60(5): 867–882. doi:10.1016/0016-7037(95)00423-8.
- Mourey AJ, Shea T, Hammer JE (2023). Preservation of Magma Recharge Signatures in Kīlauea Olivine During Protracted Storage. *Journal of Geophysical Research: Solid Earth* 128(1). doi:10.1029/2022jb025523.
- Neave DA, Stewart AG, Hartley ME, Namur O (2024). Iron valence systematics in clinopyroxene crystals from ocean island basalts. *Contributions to Mineralogy and Petrology* 179(6). doi:10.1007/s00410-024-02144-x.
- Neumann W, Henke S, Breuer D, Gail HP, Schwarz WH, Tieloff M, Hopp J, Spohn T (2018). Modeling the evolution of the parent body of acapulcoites and lodranites: A case study for partially differentiated asteroids. *Icarus* 311: 146–169. doi:10.1016/j.icarus.2018.03.024.
- Outrequin C, Alexandre A, Vallet-Coulomb C, Piel C, Devidal S, Landais A, Couapel M, Mazur JC, Peugeot C, Pierre M, Prié F, Roy J, Sonzogni C, Voigt C (2021). The triple oxygen isotope composition of phytoliths, a new proxy of atmospheric relative humidity: controls of soil water isotope composition, temperature, CO<sub>2</sub> concentration and relative humidity. *Climate of the Past* 17(5): 1881–1902. doi:10.5194/cp-17-1881-2021.
- Paton C, Woodhead JD, Hellstrom JC, Hergt JM, Greig A, Maas R (2010). Improved laser ablation U–Pb zircon geochronology through robust downhole fractionation correction. *Geochemistry, Geophysics, Geosystems* 11(3). doi:10.1029/2009gc002618.
- Patzer A, Schultz L, Franke L (2003). New noble gas data of primitive and differentiated achondrites including Northwest Africa 011 and Tafassasset. *Meteoritics & Planetary Science* 38(10): 1485–1497. doi:10.1111/j.1945-5100.2003.tb00252.x.
- Paul AN, Spikings RA, Gaynor SP (2021). U–Pb ID-TIMS reference ages and initial Pb isotope compositions for Durango and Wilberforce apatites. *Chemical Geology* 586: 120604. doi:10.1016/j.chemgeo.2021.120604.
- Pellas P, Fiéni C, Tieloff M, Jessberger EK (1997). The cooling history of the Acapulco meteorite as recorded by the <sup>244</sup>Pu and <sup>40</sup>Ar–<sup>39</sup>Ar chronometers. *Geochimica et Cosmochimica Acta* 61(16): 3477–3501. doi:10.1016/s0016-7037(97)00167-1.
- Petaev MI, Barsukova LD, Lipschutz ME, Wang M, Ariskin AA, Clayton RN, Mayeda TK (1994). The Divnoe meteorite: Petrology, chemistry, oxygen isotopes and origin. *Meteoritics* 29(2): 182–199. doi:10.1111/j.1945-5100.1994.tb00671.x.
- Peterson LD, Newcombe ME, Alexander CM, Wang J, Nielsen SG (2024). The H-poor nature of incompletely melted planetesimals: The view from acapulcoites and lodranites. *Geochimica et Cosmochimica Acta* 370: 1–14. doi:10.1016/j.gca.2024.02.002.
- Peterson LD, Newcombe ME, Alexander CM, Wang J, Nielsen SG (2025). A reconstruction of the H<sub>2</sub>O and F contents of the Erg Cech 002 parent body. *Geochimica et Cosmochimica Acta* 399: 82–92. doi:10.1016/j.gca.2025.04.009.
- Petrus JA, Kamber BS (2012). VizualAge: A Novel Approach to Laser Ablation ICP-MS U–Pb Geochronology Data Reduction. *Geostandards and Geoanalytical Research* 36(3): 247–270. doi:10.1111/j.1751-908x.2012.00158.x.
- Piralla M, Villeneuve J, Schnuriger N, Bekaert DV, Marrocchi Y (2023). A unified chronology of dust formation in the early solar system. *Icarus* 394: 115427. doi:10.1016/j.icarus.2023.115427.
- Potin S, Brissaud O, Beck P, Schmitt B, Magnard Y, Correia JJ, Rabou P, Jocou L (2018). SHADOWS: a spectro-gonio radiometer for bidirectional reflectance studies of dark meteorites and terrestrial analogs: design, calibrations, and performances on challenging surfaces. *Applied Optics* 57(28): 8279. doi:10.1364/ao.57.008279.
- Renne PR, Balco G, Ludwig KR, Mundil R, Min K (2011). Response to the comment by W.H. Schwarz et al. on “Joint determination of <sup>40</sup>K decay constants and <sup>40</sup>Ar\*/<sup>40</sup>K for the Fish Canyon sanidine standard, and improved accuracy for <sup>40</sup>Ar/<sup>39</sup>Ar geochronology” by P.R. Renne et al. (2010). *Geochimica et Cosmochimica Acta* 75(17): 5097–5100. doi:10.1016/j.gca.2011.06.021.
- Sanborn ME, Wimpenny J, Williams CD, Yamakawa A, Amelin Y, Irving AJ, Yin QZ (2019). Carbonaceous achondrites Northwest Africa 6704/6693: Milestones for early Solar System chronology and genealogy. *Geochimica et Cosmochimica Acta* 245: 577–596. doi:10.1016/j.gca.2018.10.004.
- Schoene B, Bowring SA (2007). Determining accurate temperature–time paths from U–Pb thermochronology: An example from the Kaapvaal craton, southern Africa. *Geochimica et Cosmochimica Acta* 71(1): 165–185. doi:10.1016/j.gca.2006.08.029.



- Shearer C, Burger P, Neal C, Sharp Z, Spivak-Birndorf L, Borg L, Fernandes V, Papike J, Karner J, Wadhwa M, Gaffney A, Shafer J, Geissman J, Atudorei NV, Herd C, Weiss B, King P, Crowther S, Gilmour J (2010). Non-basaltic asteroidal magmatism during the earliest stages of solar system evolution: A view from Antarctic achondrites Graves Nunatak 06128 and 06129. *Geochimica et Cosmochimica Acta* 74(3): 1172–1199. doi:10.1016/j.gca.2009.10.029.
- Smith T, He H, Li S, Su F (2023). Light noble gases in 11 achondrites: Cosmic ray exposure ages, gas retention ages, and preatmospheric sizes. *Meteoritics & Planetary Science* 58(11): 1580–1599. doi:10.1111/maps.14085.
- Srinivasan P, Dunlap DR, Agee CB, Wadhwa M, Coleff D, Ziegler K, Zeigler R, McCubbin FM (2018). Silica-rich volcanism in the early solar system dated at 4.565 Ga. *Nature Communications* 9(1). doi:10.1038/s41467-018-05501-0.
- Suavet C, Alexandre A, Franchi IA, Gattacceca J, Sonzogni C, Greenwood RC, Folco L, Rochette P (2010). Identification of the parent bodies of micrometeorites with high-precision oxygen isotope ratios. *Earth and Planetary Science Letters* 293(3–4): 313–320. doi:10.1016/j.epsl.2010.02.046.
- Sugiura N, Fujiya W (2014). Correlated accretion ages and  $\epsilon^{54}\text{Cr}$  of meteorite parent bodies and the evolution of the solar nebula. *Meteoritics & Planetary Science* 49(5): 772–787. doi:10.1111/maps.12292.
- Takeda H, Mori H, Hiroi T, Saito J (1994). Mineralogy of new Antarctic achondrites with affinity to Lodran and a model of their evolution in an asteroid. *Meteoritics* 29(6): 830–842. doi:10.1111/j.1945-5100.1994.tb01096.x.
- Tartèse R, Anand M, Franchi IA (2019). H and Cl isotope characteristics of indigenous and late hydrothermal fluids on the differentiated asteroidal parent body of Grave Nunataks 06128. *Geochimica et Cosmochimica Acta* 266: 529–543. doi:10.1016/j.gca.2019.01.024.
- Tartèse R, Gattacceca J, Avicé G, Beck P, Devouard B, Debaille V, Fawcett L, Hublet G, Joy KH, Sonzogni C, Villeneuve J (2025). Mineralogy, bulk and mineral geochemistry, geochronology, and noble gas isotope data for the Néma 001 meteorite. University of Manchester. doi:10.48420/29126567.V3.
- Toplis MJ (2005). The thermodynamics of iron and magnesium partitioning between olivine and liquid: criteria for assessing and predicting equilibrium in natural and experimental systems. *Contributions to Mineralogy and Petrology* 149(1): 22–39. doi:10.1007/s00410-004-0629-4.
- Touboul M, Kleine T, Bourdon B, Van Orman JA, Maden C, Zipfel J (2009). Hf–W thermochronometry: II. Accretion and thermal history of the acapulcoite–lodranite parent body. *Earth and Planetary Science Letters* 284(1–2): 168–178. doi:10.1016/j.epsl.2009.04.022.
- Usui T, Jones JH, Mittlefehldt DW (2015). A partial melting study of an ordinary (H) chondrite composition with application to the unique achondrite Graves Nunataks 06128 and 06129. *Meteoritics & Planetary Science* 50(4): 759–781. doi:10.1111/maps.12392.
- Vermeesch P (2018). IsoplotR: A free and open toolbox for geochronology. *Geoscience Frontiers* 9(5): 1479–1493. doi:10.1016/j.gsf.2018.04.001.
- Villeneuve J, Chaussidon M, Libourel G (2009). Homogeneous Distribution of  $^{26}\text{Al}$  in the Solar System from the Mg Isotopic Composition of Chondrules. *Science* 325(5943): 985–988. doi:10.1126/science.1173907.
- Warren PH, Rubin AE, Isa J, Brittenham S, Ahn I, Choi BG (2013). Northwest Africa 6693: A new type of FeO-rich, low- $\Delta^{17}\text{O}$ , poikilitic cumulate achondrite. *Geochimica et Cosmochimica Acta* 107: 135–154. doi:10.1016/j.gca.2012.12.025.
- Weigel A, Eugster O, Koeberl C, Michel R, Krähenbühl U, Neumann S (1999). Relationships among lodranites and acapulcoites: noble gas isotopic abundances, chemical composition, cosmic-ray exposure ages, and solar cosmic ray effects. *Geochimica et Cosmochimica Acta* 63(2): 175–192. doi:10.1016/s0016-7037(99)00012-5.
- Weiss BP, Elkins-Tanton LT (2013). Differentiated Planetesimals and the Parent Bodies of Chondrites. *Annual Review of Earth and Planetary Sciences* 41(1): 529–560. doi:10.1146/annurev-earth-040610-133520.
- Wieler R, Huber L, Busemann H, Seiler S, Leya I, Maden C, Masarik J, Meier MMM, Nagao K, Trappitsch R, Irving AJ (2016). Noble gases in 18 Martian meteorites and angrite Northwest Africa 7812—Exposure ages, trapped gases, and a re-evaluation of the evidence for solar cosmic ray-produced neon in shergottites and other achondrites. *Meteoritics & Planetary Science* 51(2): 407–428. doi:10.1111/maps.12600.
- Woodhead JD, Hergt JM (2000). Pb-Isotope Analyses of USGS Reference Materials. *Geostandards Newsletter* 24(1): 33–38. doi:10.1111/j.1751-908x.2000.tb00584.x.
- Wostbrock JA, Sharp ZD (2021). Triple Oxygen Isotopes in Silica–Water and Carbonate–Water Systems. *Reviews in Mineralogy and Geochemistry* 86(1): 367–400. doi:10.2138/rmg.2021.86.11.